



## Nano-material as an excellent catalyst for reducing a series of nitroanilines and dyes: triphosphonated ionic liquid- CuFe<sub>2</sub>O<sub>4</sub>-modified boron nitride

Vasanthakumar Arumugam<sup>a</sup>, Pavithra Sriram<sup>b</sup>, Ta-Jen Yen<sup>b</sup>, Gyanasivan Govindsamy Redhi<sup>a</sup>, Robert Moonsamy Gengan<sup>a,\*</sup>

<sup>a</sup> Department of Chemistry, Faculty of Applied Sciences, Durban University of Technology, Durban, South Africa

<sup>b</sup> Department of Materials Science and Engineering, National Tsing Hua University, Hsinchu 30013, Taiwan, ROC



### ARTICLE INFO

#### Keywords:

copper ferrite nanoparticle  
phosphonate tri-cationic ionic liquid  
partially oxidized boron nitride  
nitroaniline

### ABSTRACT

In this study a nanomaterial containing a novel tri-cationic phosphonate ionic liquid (TCPIL), copper ferrite magnetic nanoparticles (CuFe<sub>2</sub>O<sub>4</sub> NP) and partially oxidized modified boron nitride nanosheet (BNONS) was synthesized, characterized and used as an efficient catalyst to reduce a series of nitro-anilines (NAs), and dyes. Three different ionic liquids (ILs) [DABCO]<sup>+</sup>[PDOL]<sup>-</sup>, [APIC]<sup>+</sup>[PDOL]<sup>-</sup> and [PYR]<sup>+</sup>[PDOL]<sup>-</sup> were synthesized separately, characterized and used to prepare a novel TCPIL {[DABCO, PYR, APIC-PDOL]<sup>+</sup>[ATMP]<sup>-</sup>} ionic liquid. Thereafter CuFe<sub>2</sub>O<sub>4</sub> NPs and BNONS were used to synthesize the nanomaterial (TCPIL/CuFe<sub>2</sub>O<sub>4</sub>/BNONS): spectroscopic, microscopic and surface morphological studies were undertaken. The catalytic reduction of a series of NAs such as 2-nitroaniline (2-NA), 3-nitroaniline (3-NA), 4-nitroaniline (4-NA) and 4-nitro-2-phenylenediamine (4-NPDA) and dyes methylene blue (MB) and allura red (AR) in aqueous solution at ambient temperature were effective in all compounds tested: the order of reduction, based on reaction time, was 4-NPD > 4-NA > 3-NA > 2-NA. Kinetic studies indicated either zero order or pseudofirst order. The rate constant, order of the reaction, activation energy and constant ratio were also calculated for each substrate. Furthermore kinetic studies at various temperatures showed that an increase in temperature speeded the reaction whilst by increasing the amount of catalyst the reaction occurred faster. In addition, the nanomaterial was easily recovered and re-used for more than seven times with negligible loss of its catalytic activity. Moreover, it is possible to make different nanomaterial by combining different d-block metals such Zn, Pd, Pt and Mn with BNONSs for potential applications in biomedical, sensors and catalytic fields.

### 1. Introduction

Ionic liquids (ILs) are low melting salts which are a combination of cations and anions. They are used in various fields due to their outstanding physical and chemical properties such as having low melting point, zero vapor pressure, high solubility and either low or high viscosities depending on its structure. ILs are used in various applications such as a leading solvent for the green synthesis of nanomaterials [1,2], battery electrolytes [3], absorption of CO<sub>2</sub> [4,5] lignocellulosic biomass [6], biopharmaceutical applications [7], and catalyst in synthetic organic chemistry [8–10]. Recently, multi-cationic and multi-anionic compounds for the development of supramolecular ionic networks have been reported [11–13], whilst liquid exfoliated h-BN nanosheets (BNNS) have been stabilized using ILs [14]. It is reported that a combination of magnetic iron oxide NPs and ILs supported by BNNS have displayed better chemical activity than the IL's or NPs used alone

[15,16]. This is because of their higher surface area, extraordinary stability of monolayer's and the significant role of BNNS in preventing the aggregation and conductivity of NPs in ILs [15,16]. A multi-ionic ionic liquid is one that contains more than one cation linked to the same type of anion and is usually a mixture of ILs. This is commonly prepared by mixing pre-existing ILs. A 4th generation IL (4-ILs) is a new concept and is described as one that contains more than one cation linked to a single substrate that contains multiple anionic sites.

Copper NPs has received significant attention owing to their exceptional and interesting applications in catalysis, photonics, and electronics [17–19] whilst magnetic iron oxide (Fe<sub>3</sub>O<sub>4</sub>) and (Fe<sub>2</sub>O<sub>3</sub>) NPs exhibit an excellent properties in water treatment, magnetic imaging, biosensor, cell labelling and drug delivery because of their low toxicity and low cost, high chemical stability and saturation in magnetization and easy manipulation in low magnetic field [20].

Graphene and hexagonal boron nitride (h-BN) are the two most

\* Corresponding author.

E-mail address: [genganrm@dut.ac.za](mailto:genganrm@dut.ac.za) (R.M. Gengan).

important members of the layered materials family possessing hexagonal lattice structures with virtually similar physicochemical properties. However in the last decade h-BN has attracted greater attention because of its fascinating features such as wide energy band gap [21], chemical inertness [22], electrical insulating properties [23], high surface area [24], and high thermal conductivity [25]. Furthermore, h-BN is more suitable for fabrication of hybrids due to its unique physicochemical properties [26–29] and can promote organic reactions such as the adsorption of CO which is catalyzed by Pd (III) loaded onto h-BN [30]. Recent reports shows that h-BN serves as a good platform to stabilize and disperse the noble metal NPs and their oxides [31–34] whilst tannic acid and ferric ion complex modified with h-BN exhibit exceptional catalytic activity for the reduction of 4-NA. Also h-BN is used in industries for various applications such as sensors [29,35,36], energy [37,38], catalysts [39–43], antibacterial agents [44,45] and biomedical fields [31].

h-Boron nitride nanosheets and nanotubes have better chemical stability than their carbon analogues. A recent report indicated that the formation of B–N–O bond by slow and strong oxidation at high temperatures shortened the BN nanosheets [28]. Recently, researchers [46,47] have investigated the oxidized structure of 2D h-BN by a chemical oxidation method and studied the electronic properties of h-BNONS. They found that chemisorption of oxygen plays an important role in the oxidation process of h-BN sheets and in modifying the properties of h-BN [48]. Although, these approaches have shown a feasible pathway for the preparation of h-BNONS, further improvement in their electronic properties are desirable for catalytic applications. Herein, we propose the use of novel TCPILs for improving their conductivity and stability of  $\text{CuFe}_2\text{O}_4$  NP and h-BNONS nanosheets.

Generally, NAs are an important intermediate in organic synthesis, pharmaceuticals and dyeing industries. Many industries dispose of untreated effluent containing NAs thereby polluting the environment and ground-water [49]. Recently public health and environmental pollution issues are reported on low concentration of 2-NA especially in contaminated water [50–52]. The United States Environmental Protection Agency have listed the NAs as dangerous wastes and toxic pollutants [51,52]. Hence better protocols are required to convert the NAs to less toxic and more useful products. One such methodology is to use catalysts which could be effective in ambient reaction conditions and preferably in aqueous solution [53]. Such methodology is based on reduction of NAs to their corresponding amines derivatives [54,55]. Recently, researchers developed an immobilized iron metal containing IL which was used as an effective and versatile heterogeneous catalyst for the chemoselective hydrogenation of nitroarenes into anilines [56].

The present study describes the facile synthesis and full characterization of three ILs, a unique TCPILs and their utility in the preparation of the nanomaterial containing  $\text{CuFe}_2\text{O}_4$  and BNONS. Furthermore, the catalytic activity of the nanomaterial was assessed for the reduction of a series of NAs to their respective amino aromatics whilst two dyes were also included in this study. The kinetic studies of reduction reaction at different temperature and various quantity of catalyst (TCPIL/ $\text{CuFe}_2\text{O}_4$ /BNONS) was investigated and data were plotted.

## 2. Experimental

### 2.1. Materials and Method

Boron nitride (99.8% purity), copper sulphate (99.5% purity), ferric chloride (99.8% purity), ferrous sulphate (99.9% purity), liquid ammonia (30% solution), amino trimethylene triphosphonic acid (ATMP) (98% purity), 1-methyl-2-pyrrolidinone (99.8% purity), 3-chloro-1,2-propanediol (99.8% purity), 1,4-diazobicyclo[2.2.2]octane, 2-amino pyridine, methanol, ethanol, acetonitrile, sodium nitrite (99.9%), potassium permanganate (99% purity), sulphuric acid (98% purity), hydrogen peroxide (98% purity), 2-nitroaniline (98% purity), 3-nitroaniline (98% purity), 4-nitroaniline (99% purity), 4-nitro-2-

phenylenediamine, methylene blue dye (95% purity) and allura red dye (80% purity) were purchased from Sigma Aldrich, South Africa.

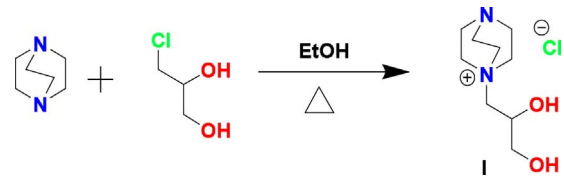
The surface morphology of the composite was investigated by JSM-6701F (JEOL, Japan) scanning electron microscope (SEM): the sample was coated with gold. The energy dispersive X-ray spectrometry (EDS) analysis was carried out using a JEM-2100F at an accelerating voltage of 200 k. The sample was dissolved in ethanol and sonicated for 10 min to disperse the NPs and to make a stable dispersion (0.1 mg/mL). A D5000 Siemens diffractometer with copper source ( $\lambda = 154.18$ ) was used for recording XRD spectra. During XRD analysis, 100 mg sample was weighed and degassed at 110 °C for 2 hrs under 140 mbar pressure. XPS spectra were obtained using an ESCALAB 250 spectrometer operated in a fixed analyzer transmission mode (pass energy 150 eV) and Al-K (1486.6 eV) excitation. Prior to AFM analysis, the composite was dissolved in ethanol and further deposited onto mica substrates and dried. Shimadzu UV-2600 instrument was calibrated and fix the required parameters then run the blank solutions before start the experiment.

### 2.1.1. Synthesis of ionic liquids

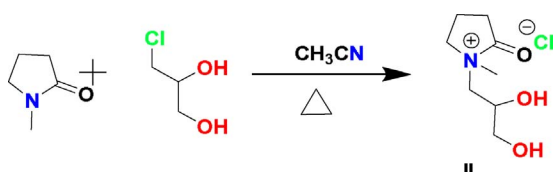
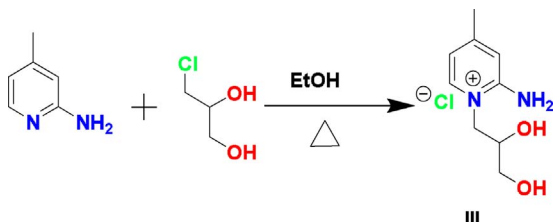
**2.1.1. I, Synthesis of  $[\text{DABCO-PDO}]^+[\text{Cl}]^-$ .** N-2', 3' dihydroxy propyl 1,4-diazobicyclo[2.2.2]octanium chloride  $[\text{DABCO-PDO}]^+[\text{Cl}]^-$  (I) IL was synthesized, characterized and purified by known protocol [57] (Scheme 1).

**2.1.1. II, Synthesis of  $[\text{PYR-PDO}]^+[\text{Cl}]^-$ .** In a 100 mL three-necked round bottom flask, fitted with a thermometer and water condenser, was added 1-methyl-2-pyrrolidinone (4.45 g, 50 mmol) in ethanol (50 mL). Thereafter 3-chloro-1,2-propanediol (6.0819 g, 55 mmol) was added slowly in an ice box set-up at the temperature of 8–10 °C with constant stirring and thereafter the content was brought to a moderate reflux to 90–100 °C on an oil bath, with constant stirring for 24 hrs. The flask was cooled and any volatile and unreacted materials were removed *in vacuo* to give a yellow colored liquid identified as N-2',3'-dihydroxy propyl-1-methyl-2-pyrrolidonium chloride  $[\text{PYR-PDO}]^+[\text{Cl}]^-$  (compound II): reaction Scheme 2. The yield of the product was 98.20% and it was characterized by techniques such as FTIR,  $^1\text{H}$ NMR,  $^{13}\text{C}$ NMR and elemental analyses.  $[\text{PYR-PDO}]^+[\text{Cl}]^-$ . FTIR ( $\nu = \text{cm}^{-1}$ ): 3309, 2940, 2871, 1644, 1505, 1407, 1304, 1262 and 1036.  $^1\text{H}$  NMR (400 MHz,  $\text{CDCl}_3$ ):  $\delta$  4.3 (s, 2H), 3.8 (s, 1H), 3.7 (d, 2H), 3.4–3.6 (m, 2H), 3.3 (d, 2H), 2.7 (s, 3H), 2.2 (t, 2H), (1.9–2.0 (m, 2H).  $^{13}\text{C}$  NMR (100 MHz,  $\text{CDCl}_3$ ):  $\delta$  158, 135, 132, 130, 125, 88, 25, 15. The elemental composition (%) calculated for  $\text{C}_8\text{H}_{16}\text{ClNO}_3$  is: C, 45.83; H, 7.69; N, 6.68, which are close to the values found: C, 45.56; H, 7.10; N, 6.29.

**2.1.1. III, Synthesis of  $[\text{APIC-PDO}]^+[\text{Cl}]^-$ .** In a 100 mL three-necked round bottom flask, fitted with a thermometer and water condenser, was added 2-amino pyridine (APIC) (4.57 g, 50 mmol) in ethanol (50 mL). Thereafter 3-chloro-1,2-propanediol (6.0819 g, 55 mmol) was added slowly in an ice box setup at the temperature of 8–10 °C with constant stirring and the content was brought to a moderate reflux to 90–100 °C on an oil bath, with constant stirring for 24 hrs. The flask was cooled and volatile unreacted materials were removed *in vacuo* to give a yellow colored N-2',3'- dihydroxy propyl 2-amino pyridinium chloride  $[\text{APIC-PDO}]^+[\text{Cl}]^-$  ionic liquid (compound III) shown in reaction Scheme 3. The yield of the product was 96% and it was



Scheme 1. Synthesis of  $[\text{DABCO-PDO}]^+[\text{Cl}]^-$ .

Scheme 2. Synthesis of  $[\text{PYR-PDO}]^+[\text{Cl}]^-$ .Scheme 3. Synthesis of  $[\text{APIC-PDO}]^+[\text{Cl}]^-$ .

characterized by the following techniques FTIR,  $^1\text{H}$ NMR,  $^{13}\text{C}$ NMR and elemental analyses.  $[\text{APIC-PDO}]^+[\text{Cl}]^-$ . FTIR ( $\nu = \text{cm}^{-1}$ ): 3323, 3170, 2953, 2884, 1583, 1444, 1373, 1046 and 1034.  $^1\text{H}$  NMR (400 MHz,  $\text{CD}_3\text{OD}$ ): 8 7.8 (d, 1H), 7.0 (s, 1H), 6.8 (d, 1H), 4.5–4.6 (d, 1H), 4.2–4.4 (d, 1H), 4.0–4.1 (d, 1H), 3.5–3.8 (m, 2H), 2.5–3.0 (s, 3H).  $^{13}\text{C}$  NMR (100 MHz,  $\text{CD}_3\text{OD}$ ): 8 156, 142, 118, 115, 70, 65, 55, 22. The elemental composition (%) calculated for  $\text{C}_9\text{H}_{15}\text{ClN}_2\text{O}_2$  is: C, 49.43; H, 6.91; N, 12.81, which are close to the values found: C, 49.56; H, 6.60; N, 12.59.

**2.1.1.4. IV, Synthesis of  $[\text{DABCO, PYR, APIC-PDO}]^+[\text{ATMP}]^-$ .** In a 100 mL three-necked round bottom flask, fitted with a thermometer and water condenser, was added a sodium hydroxide (0.4 g, 20 mmol) in 50 mL of methanol. Thereafter amino tris (methyl phosphonic acid) (ATMP) (5.981 g, 20 mmol) was added dropwise, with constant stirring, on an ice bath. The reaction mixture was maintained at 8–10 °C for 1 h. Then 20 mmol of each  $[\text{DABCO-PDO}]^+[\text{Cl}]^-$ ,  $[\text{PYR-PDO}]^+[\text{Cl}]^-$  and  $[\text{APIC-PDO}]^+[\text{Cl}]^-$  IL were added. The flask was transferred into an oil bath and the content was brought to reflux at 120 °C for 24 hrs. The flask was cooled and any volatile and unreacted materials were removed *in vacuo* to give a yellow colored  $[\text{DABCO, PYR, APIC-PDO}]^+[\text{ATMP}]^-$  ionic liquid (**compound IV**) which was subsequently further purified by solvent washing, reaction Scheme 4. The yield of the product was 85% and it was characterized by the following techniques: FTIR,  $^1\text{H}$ NMR,  $^{13}\text{C}$ NMR,  $^{31}\text{P}$ NMR and elemental analysis.  $[\text{DABCO, PYR, APIC-PDO}]^+[\text{ATMP}]^-$ . FTIR ( $\nu = \text{cm}^{-1}$ ): 3416, 3323, 2953, 2884, 1744, 1658, 1513, 1453, 1382, 1243, 1182, 1034, 915, 736, 654 and 569 (see Fig. 1b).  $^1\text{H}$  NMR (400 MHz,  $\text{D}_2\text{O}$ ): 8 7.5 (d, 2H), 6.6–6.8 (m, 3H), 4.3–4.4 (s, 2H), 4.0–4.1 (s, 6H), 3.9–4.0 (t, 5H), 3.8–3.9 (m, 10H), 3.5–3.7 (m, 23H), 3.3–3.4 (t, 2H), 3.1–3.2 (s, 3H), 2.2–2.4 (m, 6H), 1.7–2.1 (m, 2H).  $^{13}\text{C}$  NMR (100 MHz,  $\text{D}_2\text{O}$ ): 8 180, 160, 155, 145, 135, 118, 72, 68, 67, 65, 64, 63, 62, 61, 58, 56, 55, 54, 53, 52, 50, 48, 46, 32, 30, 22, 18.

### 2.1.2. Synthesis of $\text{CuFe}_2\text{O}_4$ nanoparticles

Magnetic  $\text{CuFe}_2\text{O}_4$  nanoparticles were synthesized by chemical co-precipitation of  $\text{Fe}^{3+}$  and  $\text{Cu}^{2+}$  ions in an alkaline solution, followed by treatment under hydrothermal conditions [58,59].

### 2.1.3. Preparation of partially oxidized BNONS

The BNONS was prepared by modifying the chemical oxidation method [46,48]. Briefly, h-BN powder (1 g, 40 mmol) was added to a solution of sodium nitrite (0.8 g), in concentrated sulphuric acid (50 mL), on an ice bath. Thereafter potassium permanganate (5.6 g) was added, vigorously stirred and maintained at 10 °C. The reaction vessel was removed from the ice bath, agitated for 3 hrs and heated at 40 °C. Then deionized water (100 mL) was subsequently added, the

reaction vessel was transferred to an oil bath and heated at 120–130 °C for 45 minutes. The solution was diluted with 200 mL of deionized water followed by the addition of a 30% solution of hydrogen peroxide (50 mL). The as-obtained partially oxidized BNONS powder (white color) was repeatedly washed with deionized water and dilute HCl to remove sulphate ions. The final washings were tested with  $\text{BaCl}_2$  solution for sulphate. The as-purified partially oxidized BN (BNONS) powder was filtered and dried at 60 °C for 24 hrs.

### 2.1.4. Preparation of nanomaterial

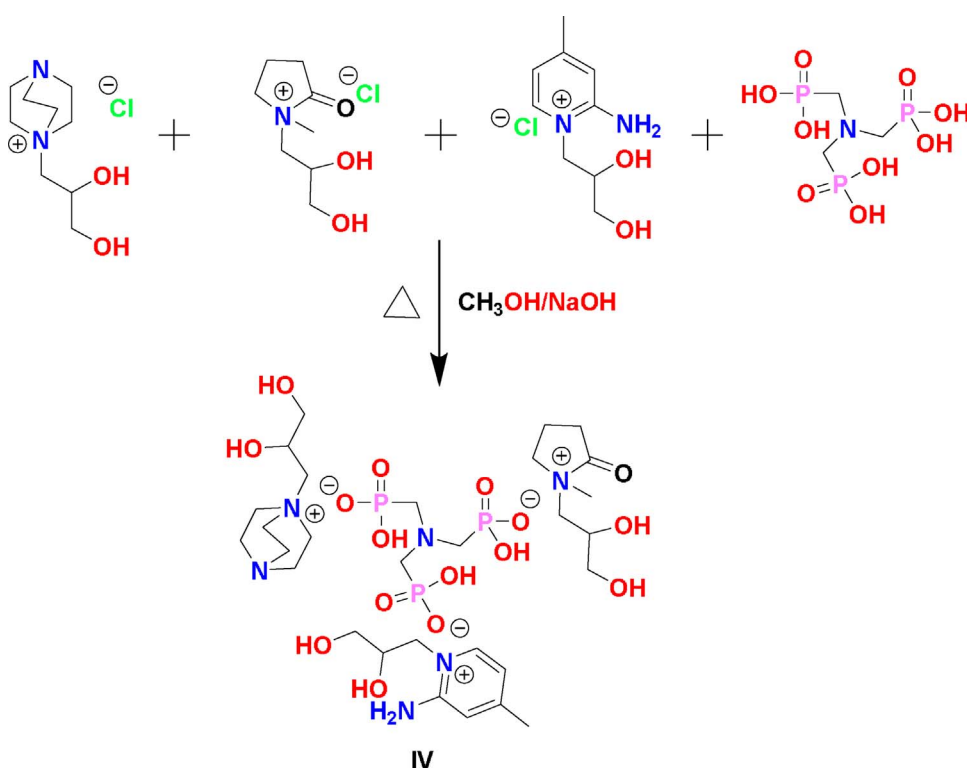
The TCPIL/ $\text{CuFe}_2\text{O}_4$ /BNONS nanomaterial (See Fig. 1) was synthesized by co-precipitation of the as-prepared TCPIL/ $\text{CuFe}_2\text{O}_4$  nanoparticles in BNONS aqueous solution. In a typical synthesis, 1 g of TCPIL  $\{[(\text{DABCO-PYR-APIC})\text{-PDOL}]^+[\text{ATMP}]^-\}$  was dissolved in deionized water (20 mL). Then,  $\text{CuFe}_2\text{O}_4$  (2 g) NPs was added into the above solution and heated at 120 °C for 24 hrs with constant stirring. Thereafter sodium dodecyl lauryl sulfate (0.1 g) was added followed by addition of BNONS solution (1.0 g in 10 mL) and 30% ammonia solution (25 mL) with vigorous stirring to dissolve all materials. This solution was heated at 150 °C with constant stirring for 12 hrs. Then the pH of the solution was adjusted to 9–10 with dilute ammonia solution. The mixture was stirred for 1 h and cooled to reach ambient temperature. Finally, the mixture was centrifuged and filtered to obtain TCPIL/ $\text{CuFe}_2\text{O}_4$ /BNONS powder (brown). The product was washed several times with deionized water and dried under vacuum at 70 °C. The final product was dispersed in ethanol (20 mL). The mass ratio of  $\text{CuFe}_2\text{O}_4$ , IL and BNONS in the TCPIL/ $\text{CuFe}_2\text{O}_4$ /BNONS nanomaterial was calculated as 2:1:1. The outline method of the preparation shown in Fig. 1 as below.

### 2.1.5. Catalytic reduction of nitroanilines and dyes

The catalytic activity of TCPIL/ $\text{CuFe}_2\text{O}_4$ /BNONS was investigated by the reduction of a series of NAs and dyes (Scheme 5). Briefly, 2-NA (0.5 mL, 0.05 M), 3-NA (0.75 mL, 0.05 M), 4-NA (0.75, 0.01 M), 4-NPDA (0.75, 0.005 M) as well as MB (0.75, 0.01 M) and AR (0.50 mL, 0.05 M) solution was added separately into a quartz cuvette followed by  $\text{NaBH}_4$  (0.75 mL, 0.5 M) and finally by deionized water (1.485 mL). A smaller quantity of 4-NPDA was used due to its poor solubility. Then an aqueous solution of TCPIL/ $\text{CuFe}_2\text{O}_4$ /BNONS (0.015 mL, 0.2 mg/mL) was added into the quartz cuvette and the reaction was monitored by UV-Vis. The UV-vis absorption spectra were recorded after every five minutes (Fig. 11(a)–(f)). The kinetics of the reaction was investigated to compute the rate constant, order of the reaction and activation energy. In addition, several temperatures such as 298 K, 303 K, 313 K, 323 K, 333 K and different dosage of the catalyst such as 0.015, 0.030 and 0.040 (2 mg/ml) were used for kinetic studies. During the reduction of NAs and dyes, the solution changed to colourless thereby indicating a visual confirmation of the reduction process. After completion of the reaction, small aliquots of  $\text{NH}_4\text{Cl}$  solution was added to neutralize excess  $\text{NaBH}_4$ . The catalyst was recovered by external magnets as shown in Fig. 2.

## 3. Results and Discussion

The FTIR spectrum of TCPIL/ $\text{CuFe}_2\text{O}_4$ /BNONS nanomaterial (Figure ES-1a (Electronic Supplementary)) showed the characteristic peaks at 3317, 2910, 1762, 1620, 1398, 1058, 808, and 559  $\text{cm}^{-1}$ , revealing the presence of functional groups such as  $-\text{NH}_2$ ,  $-\text{C-H}$ ,  $-\text{C=O}$ ,  $-\text{C-N}$ ,  $-\text{C-O}$ ,  $-\text{PO}_3$ ,  $-\text{B-N}$  and  $\text{FeO}$ . In addition to these peaks,  $\text{C-H}$  and  $-\text{OH}$  peaks were also observed at 2910  $\text{cm}^{-1}$  and 3317  $\text{cm}^{-1}$ , respectively. The BNONS (Figure ES-1c) showed surface bonds such as  $\text{B-N}$  (1446  $\text{cm}^{-1}$ ),  $\text{B-OH/B-NH}_2$  (3325  $\text{cm}^{-1}$  and 3190  $\text{cm}^{-1}$ ),  $\text{B-N-B}$  (802  $\text{cm}^{-1}$ ),  $\text{B-N-O}$  (1107  $\text{cm}^{-1}$ ),  $\text{C-O}$  (1045  $\text{cm}^{-1}$ ), and  $\text{B-N-O}$  (1026  $\text{cm}^{-1}$ ) [31]. FTIR results showed that non-covalent functionalization of BNONS occurred via van der Waals forces as consistent with a previous report [60]. When compared to the pristine h-BN, the band at



**Scheme 4.** Synthesis of  $[DABCO, PYR, APIC-PDO]^{+}[ATMP]^{-}$ .

$1100\text{ cm}^{-1}$  for OH-BNONS shifted slightly. Furthermore, the absorption peak was assigned to B–O deformation originating from the hydroxyl group of the OH–BNONS [31]. The absorption peaks were in correlation with those reported previously for activated BN [61]. The FTIR of nanomaterial also exhibited typical absorption bands at 925 and  $970\text{ cm}^{-1}$  corresponding to the stretching vibrations of the P–OH group in IL shown in (Figure ES-1b and 1d). The characteristic peaks of  $\text{PO}_3\text{H}$  were also observed at 1762, 1620 and  $1058\text{ cm}^{-1}$  [61]. The characteristic absorption band of Fe–O in  $\text{CuFe}_2\text{O}_4$  NP were observed at 559 and  $466\text{ cm}^{-1}$ . In addition, peaks at 1629, 1539, 1338 and  $950\text{ cm}^{-1}$  corresponded to metal–metal and metal oxygen bonds. Regarding the IL to metal and BN–P vibrations, the stretching vibration of the Cu–N bonds were also observed at  $456\text{ cm}^{-1}$ .

X-ray diffraction (XRD) analysis was an important technique which provided valuable information for interpretation of the crystalline nature of the metal, metal oxide and BNONS. The typical XRD pattern of the TCPIL/ $\text{CuFe}_2\text{O}_4$ /BNONS nanomaterial (Figure ES-2) displayed

two characteristic peaks at the  $2\Theta$  values of  $27.3^{\circ}$  and  $55.3^{\circ}$  for (212), (423) planes, which corresponded to the two crystalline phases such as hexagonal BNONS (JCPDS 45-896) and cubic  $\text{CuFe}_2\text{O}_4$  (JCPDS 77-10). The  $\text{CuFe}_2\text{O}_4$  phase exhibited sharp peaks at  $2\Theta$  value of  $311$ , suggesting they were nano-crystalline. The other phases such as copper (JCPDS, no. 851326); copper (I) oxide,  $\text{Cu}_2\text{O}$  (JCPDS, no. 741230); copper (II) oxide,  $\text{CuO}$  (JCPDS, no. 410254); and magnetite,  $\text{Fe}_3\text{O}_4$  (JCPDS, no. 751609) were also observed. By using the formula of Debye Scherrer ( $D = K\lambda/(\beta \cos\theta)$ ) and the full width at half maximum of the diffraction peak at the Bragg angle  $2\theta$ , the size of  $\text{CuFe}_2\text{O}_4$  was determined to be 20 nm. The crystallinity of  $\text{CuFe}_2\text{O}_4$ NP in the composite was confirmed by XRD patterns. Figure ES 2 shows discrete characteristic peaks at the  $2\Theta$  values of  $27.3^{\circ}$ ,  $28.4^{\circ}$ ,  $32.9^{\circ}$ ,  $46.8^{\circ}$ ,  $55.3^{\circ}$  and  $58.0^{\circ}$  which were assigned to the (220), (117), (1114), (311) (552) and (443) crystallographic planes of  $\text{Fe}_3\text{O}_4$ . The XRD peaks of  $\text{Fe}_3\text{O}_4$  at around  $26.8^{\circ}$  and  $55.6^{\circ}$  overlapped with the (220) and (443) facets of the h-BN.

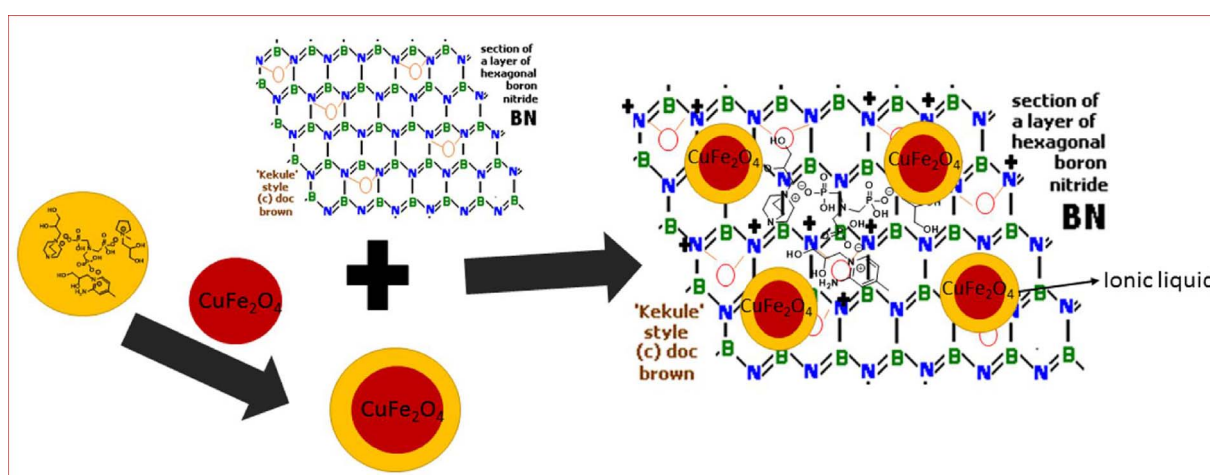
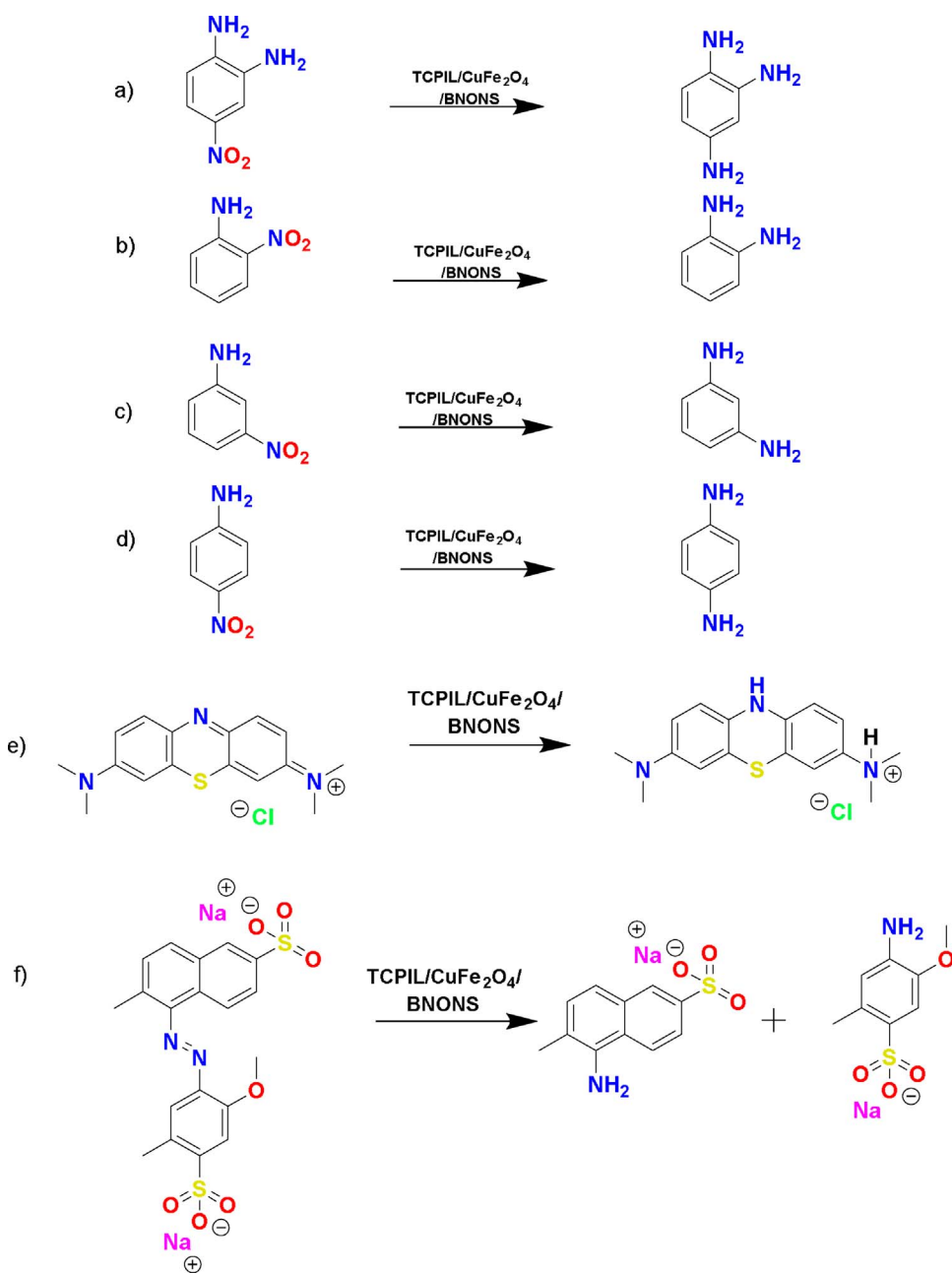


**Fig. 1.** Preparation of TCPIL/ $\text{CuFe}_2\text{O}_4$ /BNONS Nanomaterial.



**Scheme 5.** Reduction of various NAs such as (a) 4-NPDA, (b) 2-NA, (c) 3-NA (d) 4-NA and dyes (e) MB and (f) AR to their amine and corresponding analogues.

Raman spectra provided useful information to identify the bonding states of the h-BN films, thus providing complementary evidence of the successful formation of modified h-BN [31,46,60,62]. The characteristics peaks in the Raman spectra of h-BN were similar to that of the BCN film prior to etching, revealing that B and N atoms were dominating the edge effect. The greatly imperfect  $SP_2$  hybridized graphene-like structure of BN on Cu foil was observed. The  $E_{2g}$  symmetric vibration mode in h-BN indicated the peaks at 1365 and 1872  $cm^{-1}$  which were similar to that of h-BN (Fig. 3b) [63–65]. Subsequently, the additional sharp peak at 1707  $cm^{-1}$  indicated the B-O-N bond. The Raman spectra of h-BNONS (Fig. 3a) exhibited some extra peaks corresponding to oxygen coordinated boron and nitrogen. The intensity of the peak at 1707  $cm^{-1}$  (806) was close to the peak at 1872  $cm^{-1}$  (662.5), providing ample evidence for the formation of h-BNONS. The arrangement of layers of h-BNONS was different from normal h-BN, due to the interaction of oxygen with boron and nitrogen.

Those interactions create an angle strain and some steric hindrances or slight distraction of the electronic cloud of h-BN. As a result, some of

the layers were perpendicularly allocated as shown in Fig. 9a and b. Although it does not cause any significant change in the overall structure of the h-BN, slight modification in the surface of the h-BN material occurred. The SEM images (Fig. 9a) showed the multilayers of the material. Further investigation of the SEM images revealed each layer was a single crystal. Thus, Raman spectra results clearly indicated the crystallinity level in the sample and Full Width at Half Maximum (FWHM).

X-ray photoelectron spectroscopy (XPS) was used to investigate the surface chemical composition of the TCPIL/CuFe<sub>2</sub>O<sub>4</sub>/BNONS. Fig. 4 shows the survey scan of the XPS spectrum which evidently indicates the presence of elements such as boron, nitrogen, oxygen, phosphorus, carbon, copper and iron. The exact spectra and peak area intensity were obtained by subtracting the Shirley type backgrounds for all. The deconvoluted B<sub>1s</sub>, C<sub>1s</sub> and N<sub>1s</sub> spectra are displayed in The B<sub>1s</sub> spectrum (Fig. 4b) has the peaks at the binding energy (B.E) values of 191.0 and 189.9 eV, which were attributed to B-N and B-C bonding, respectively, while the peak at 192.1 eV showed the existence of BNONS. The curve

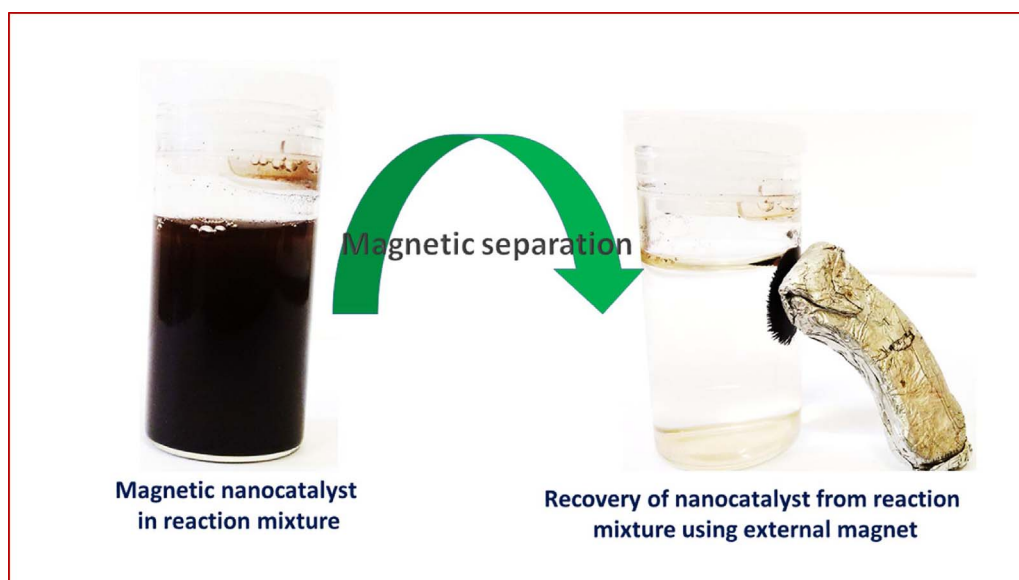


Fig. 2. Magnetic separation of TCPIL/CuFe<sub>2</sub>O<sub>4</sub>/BNONS Nanomaterial.

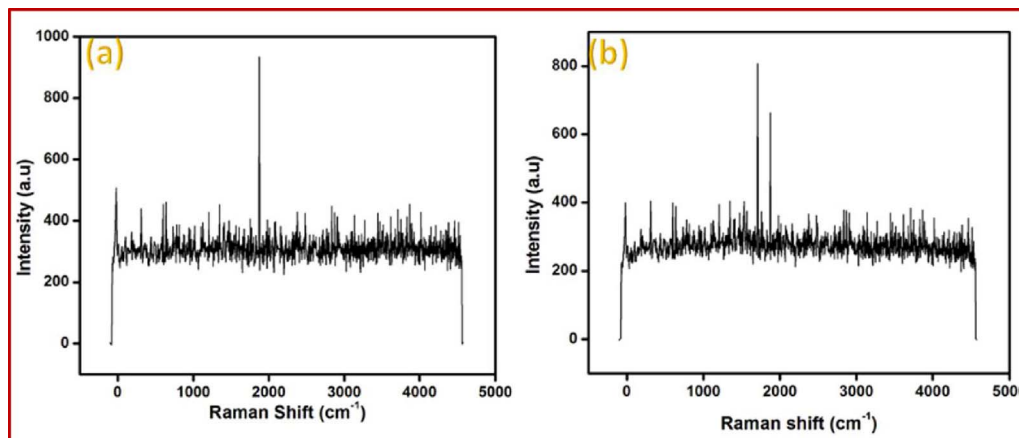


Fig. 3. Raman spectra of pure BN (3a) and partially oxidized slightly modified h-BNONS nanosheet (3b).

fitted C<sub>1s</sub> spectrum and displayed two main peaks at 284.8 and 285.8 eV, which were ascribed to C-C and C-N, respectively (Fig. 4c) [66–68]. The deconvoluted N<sub>1s</sub> spectra showed two peaks at 398.4 and 398.9 eV (Fig. 4d). The former one was attributed to N-B bonding and the latter one was ascribed to the N-C bonding [69]. The TEM, XRD and XPS results confirmed that BNONS coating was successfully prepared on the TCPIL/CuFe<sub>2</sub>O<sub>4</sub> surface via the direct impregnation method. Meanwhile, the surface modification of TCPIL/CuFe<sub>2</sub>O<sub>4</sub> by BNONS formed rich hydroxyl and phosphonate groups on the surface of the nanomaterials, which improves the surface area and dispersing ability of TCPIL/CuFe<sub>2</sub>O<sub>4</sub>/BNONS matrix.

In general, the BN nanomaterials have thin sheets with less than 8–10 layers and lateral size of the nanosheets ranges from 1.5 to 2  $\mu$ m. Fig. 5a and b displays the AFM images of TCPIL/CuFe<sub>2</sub>O<sub>4</sub>/BNONS with different height profiles (50 and 500 nm). The height profile of the nano-sheets revealed that they have multilayered nano-sheets and their thickness were  $\sim$  2.5 nm and this information was further confirmed from literature.<sup>71</sup> It has been reported that there were no wrinkles on the surfaces of the CVD-grown BNONS even after transferring to substrate [70,71].

Fig. 6a and b, shows the characteristic low-magnification TEM images of the TCPIL/CuFe<sub>2</sub>O<sub>4</sub>/BNONS nanomaterials. The CuFe<sub>2</sub>O<sub>4</sub> NP and TCPIL were uniformly spread over the BN modified partially oxidized BNONS that have fairly rough surfaces. The thickness of the BNONS are  $\sim$  2.5 nm, which was consistent with our AFM results. The

average size of CuFe<sub>2</sub>O<sub>4</sub> NP is 20 nm. The TCPIL/CuFe<sub>2</sub>O<sub>4</sub> NPs were anchored on the BNONS without forming any aggregates. TEM images showed that some of the nano layers of BNONS were arranged in parallel in comparison with that of normal h-BN. These arrangements actually give a compact space for nanoparticles and IL binding. The combination of CuFe<sub>2</sub>O<sub>4</sub> NP, ILs and BNONS should provide good catalytic efficiency.

Fig. 7a and b shows single nanosheets in the composites. The HRTEM images of the nanomaterial revealed that BNONS have multilayered sheets with an outer diameter and thickness of  $\sim$  20 nm and  $\sim$  2.5 nm, respectively. Actually, the HRTEM images are not clear due to more electron concentration and ILs interferes while focusing on microscope. However, the diameter of the nanosheets in the BNONS increased to 20–50 nm after IL modification, confirming the coating of IL on the surfaces of BNONS. The thickness of the few layers in the BNONS was around 2.5 nm as confirmed from the height profile AFM image as described previously (Fig. 5a and b). Furthermore, the TCPIL/CuFe<sub>2</sub>O<sub>4</sub>/BNONS retained their perfect crystallization after coating with TCPIL/CuFe<sub>2</sub>O<sub>4</sub> as observed from TEM images. As shown in Figure. ES-4a the distance between the two lattices fringes in the TCPIL/CuFe<sub>2</sub>O<sub>4</sub>/BNONS nanomaterial were determined to be  $\sim$  0.5 nm, which corresponds to the 311 plane of the CuFe<sub>2</sub>O<sub>4</sub> crystal (Fig. 9b). The low accelerating voltage of 60 KV was enough to perform high-angle annular dark-field scanning transmission electron microscopy (STEM) and to avoid the structural damage by the electron beam.

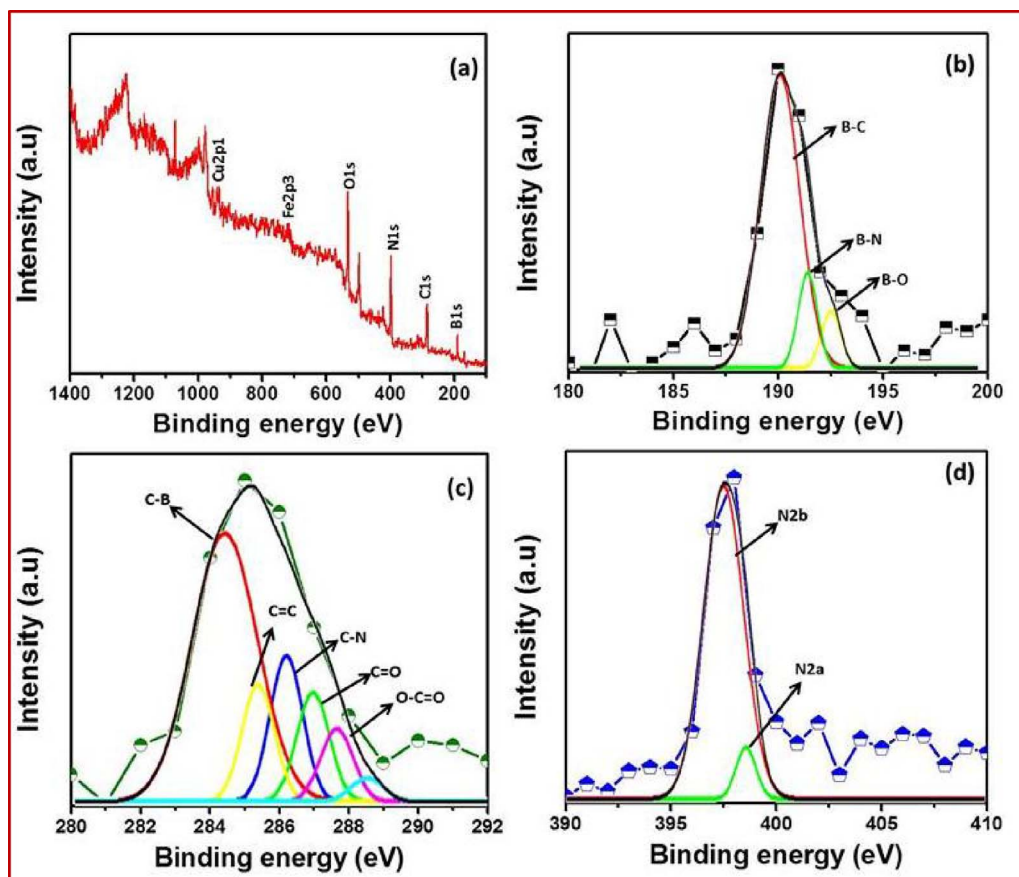


Fig. 4. 4a) XPS spectra of TCPIL/CuFe<sub>2</sub>O<sub>4</sub>/BNONS nanomaterial. 4b) The B1 s spectrum of the peaks at the binding energy (B.E), 4c) C–C and C–N binding energies, 4d) N1 s spectrum of the nanomaterial.

From the representative bright-field image, shown in Fig. 8a, it was clearly observed that the particles are irregular spheres with an average diameter of 20–50 nm. The CuFe<sub>2</sub>O<sub>4</sub> NPs appear black as indicated by the CuFe<sub>2</sub>O<sub>4</sub> and Cu NPs in Fig. 8a and b with arrows. Cu NPs appeared as bright dots due to the greater electronic conductivity of Cu than Fe. The AC-STEM images of TCPIL/CuFe<sub>2</sub>O<sub>4</sub>/BNONS and the

corresponding elemental distribution of Cu and Fe clearly showed that most of the Cu NPs were grown near the edges of the BNONS where Fe<sub>2</sub>O<sub>4</sub> NPs were present. STEM image, displayed in Fig. 8b, confirmed that CuFe<sub>2</sub>O<sub>4</sub> NP were uniformly modified onto the iron oxide surface.

Fascinatingly, analysis of the selected area electron diffraction (ED) patterns establish the differences between the nanomaterial and two

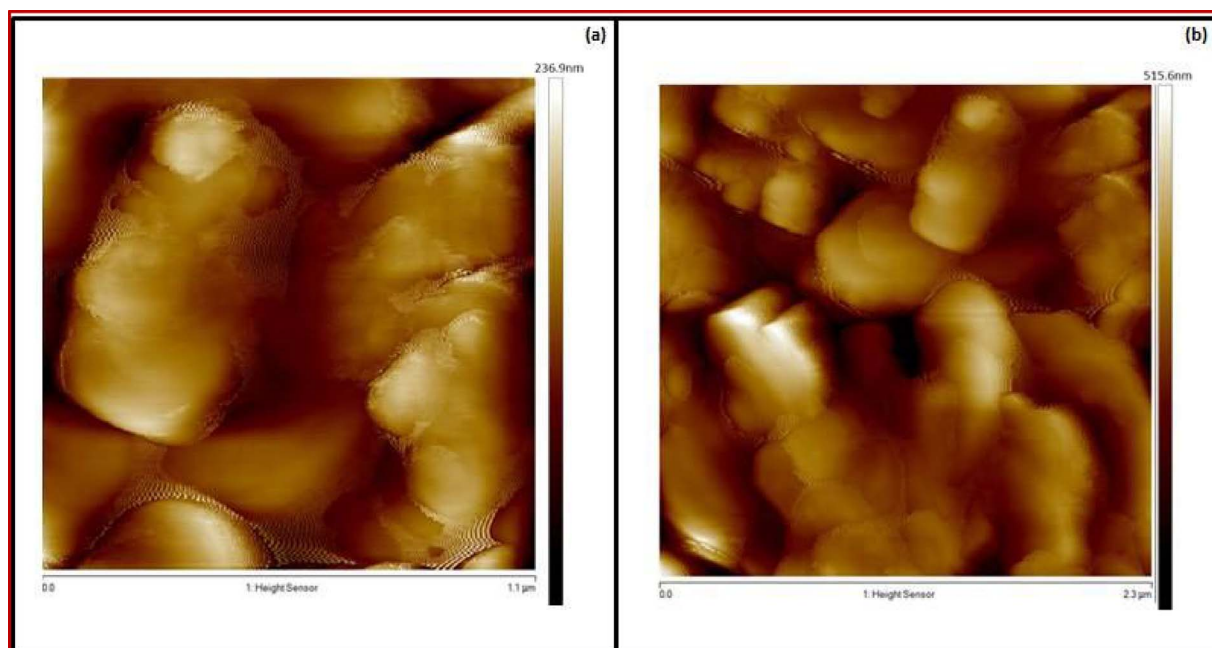


Fig. 5. AFM images of TCPIL/CuFe<sub>2</sub>O<sub>4</sub>/BNONS nanomaterial (4a–4b).

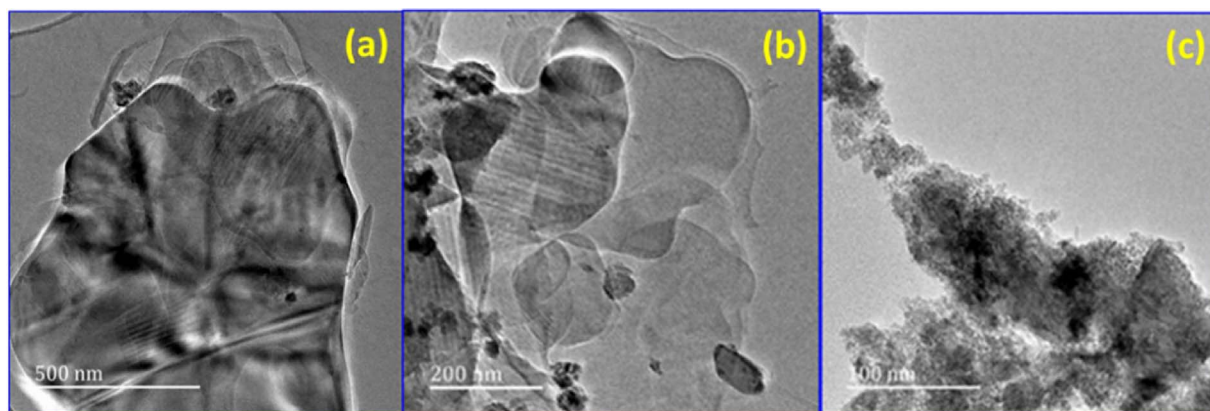


Fig. 6. TEM images of PTCIL/CuFe<sub>2</sub>O<sub>4</sub>/BNONS nanomaterial taken at different magnifications (a–b). TEM images of pure CuFe<sub>2</sub>O<sub>4</sub> nanoparticles (c).

constituents. Figures ES-3a and ES-3b shows the ED patterns of IL/CuFe<sub>2</sub>O<sub>4</sub>/BNONS nanomaterial and the CuFe<sub>2</sub>O<sub>4</sub> NP, respectively. The presence of rings in ED pattern showed the polycrystalline nature of the CuFe<sub>2</sub>O<sub>4</sub> NPs. The hexagonal ED pattern of TCPIL/CuFe<sub>2</sub>O<sub>4</sub>/BNONS nanomaterial showed the single crystalline nature. Compared to the CuFe<sub>2</sub>O<sub>4</sub> NP, ED pattern of the composite showed more bright spots due to greater electronic conductivity resulting from IL and BNONS, revealing the formation of the TCPIL/CuFe<sub>2</sub>O<sub>4</sub>/BNONS nanomaterial.

The surface morphology and particle size of the synthesized nanomaterial were additionally investigated using SEM and EDS, with the results shown in Fig. 9a, b and Fig. 10, respectively. The SEM images of the CuFe<sub>2</sub>O<sub>4</sub> NPs revealed that the NPs were densely packed with a grain size in the range of 20–30 nm. The BNONS were composed and the sheets have layered thin platelet morphology. The distribution of the CuFe<sub>2</sub>O<sub>4</sub>/IL on the TCPIL/CuFe<sub>2</sub>O<sub>4</sub>/BNONS nanomaterial surface was clearly seen, with the size of the NPs and ILs similar and were uniformly spread over the BNONS layer. This confirmed the presence of the BNONS, IL, and CuFe<sub>2</sub>O<sub>4</sub> NP in the TCPIL/CuFe<sub>2</sub>O<sub>4</sub>/BNONS nanomaterial. Further investigation of the EDS indicated the presence of elements such as B, N, C, O, P, Fe and Cu in the nanomaterial (Fig. 10). Table 1 lists the amounts of B, N, C, O, P, Fe and Cu in the nanomaterial. The mapping of elements in the nanomaterial using SEM & EDS revealed the distribution of B, N, C, O, P, Fe and Cu (Fig. 9b and c). The thermal stability of the nanomaterial was investigated by TGA analysis as shown in Fig. 11. There was no significant weight loss up to 700 °C, revealing the good thermal stability of the nanomaterial. The decomposition profile of the material was also compared to BN sheets. The nanomaterial exhibited three distinct steps of weight losses upon heating from room temperature to 1000 °C under air flow as displayed in both TG-DTG curves (Fig. 11). The first weight loss (ca. 8.0%) at

100 °C was attributed to the removal of moisture. The second weight loss at 250 °C (ca. 12%) was due to the pyrolysis of the oxygenated functional group on the BNONS surface. Interestingly, compared to normal BN, the decomposition temperature (at 200 °C) of the oxygen functional groups in material increased, suggesting the BNONS and the IL moieties were stabilized mutually. Final weight loss at 700 °C (ca. 12%) was attributed to the decomposition of the IL moiety in the BNONS layer. The results represented indirect proof for the covalent linkage of the Cu ferrite magnetic NPs and BNONS through the phosphonate IL linker. In this study, h-BN surface modified with partially oxidized BN nanosheets were prepared for the first time. This investigation developed the modified graphene oxidized method because BN underwent low and strong oxidation at high temperature to create the interaction between oxygen and the B-N bond and to reduce the electron cloud in-between the B-N. The modified BNONS was confirmed by FTIR, Raman spectroscopy and XRD. Those spectra exhibit different peaks compared to normal hexagonal BN. The physical nature of the material was also different from the normal h-BN due to its smooth texture. The surface morphology of the partially oxidized boron nitride nanosheets was changed from normal h-BN due to the angle and position of some of the sheets were changed to perpendicular. So, random sheets position arrangement perpendicular and the normal surface area could help to increase the stability and it gives some space for IL bound CuFe<sub>2</sub>O<sub>4</sub> NP and thus it was used as a base material for the nanomaterial. Another important aspect was the synthesis of novel tri-cationic phosphonate ILs, which contains DABCO, amino picoline and pyrrolidonium cations coordinated with triphosphonated amino trimethylene amino phosphonate (ATMP) based anions. The chemical compounds such as heterocyclic compounds, organic components, and substituted propane diol groups does help ILs to bind efficiently with BNONS and

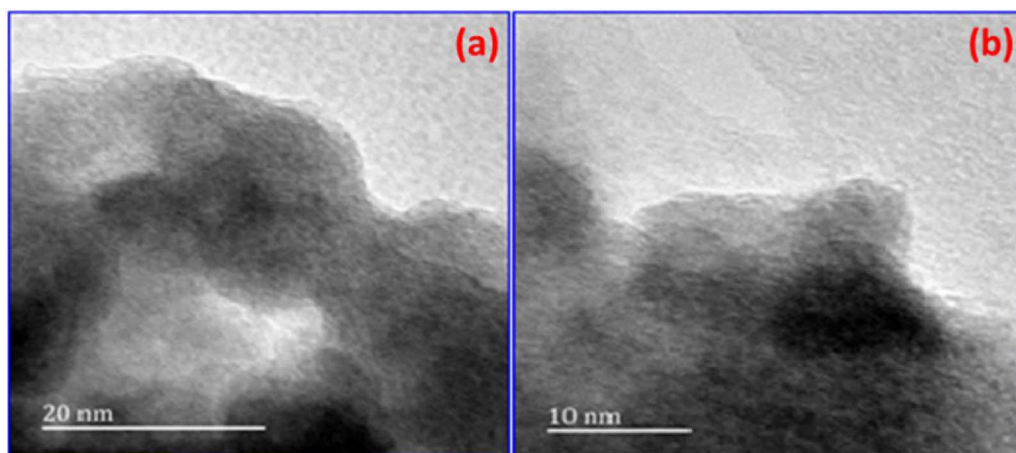


Fig. 7. HRTEM images of PTCIL/CuFe<sub>2</sub>O<sub>4</sub>/BNONS nanomaterial at (a) 20 nm and (b) 10 nm.

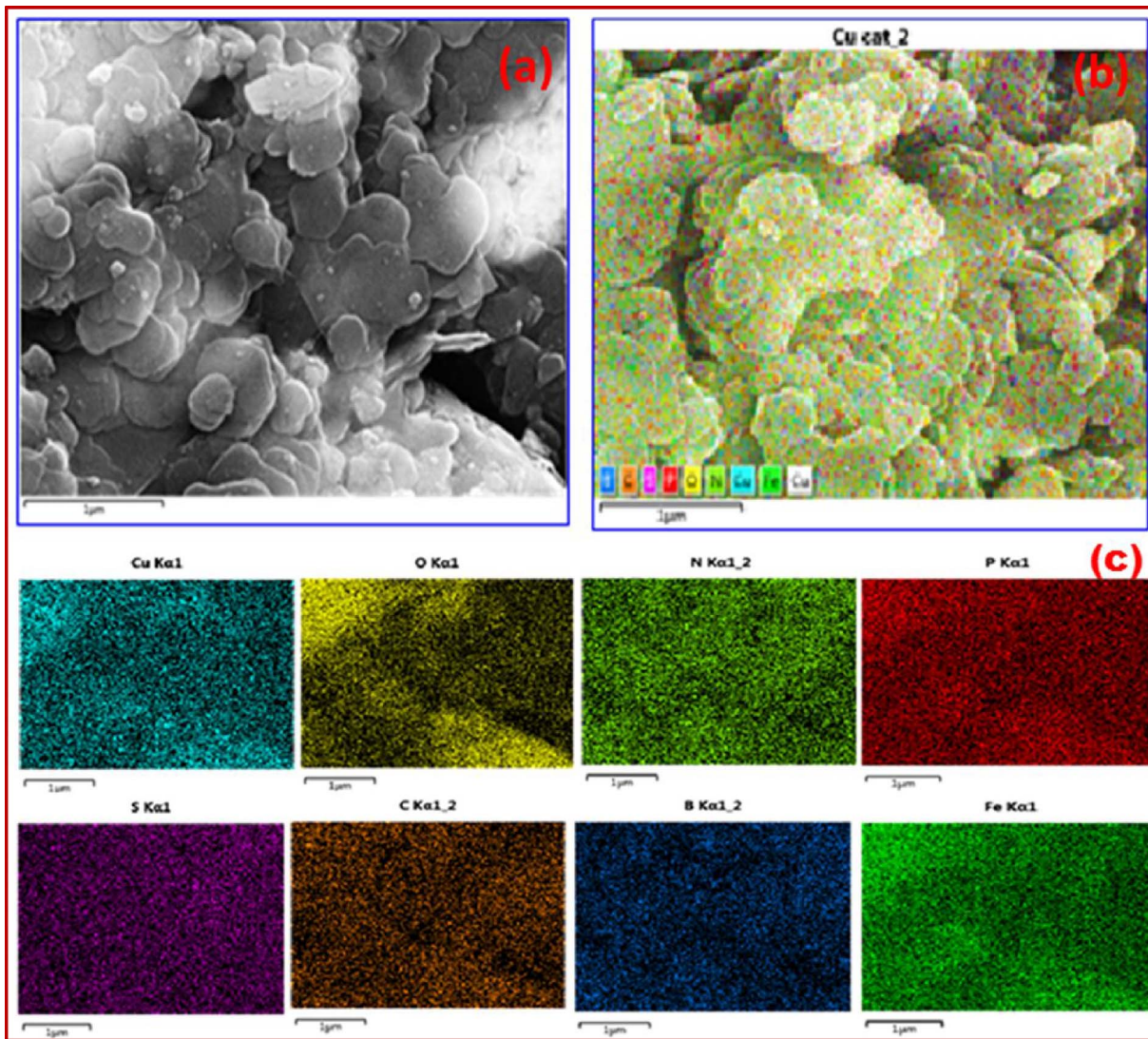
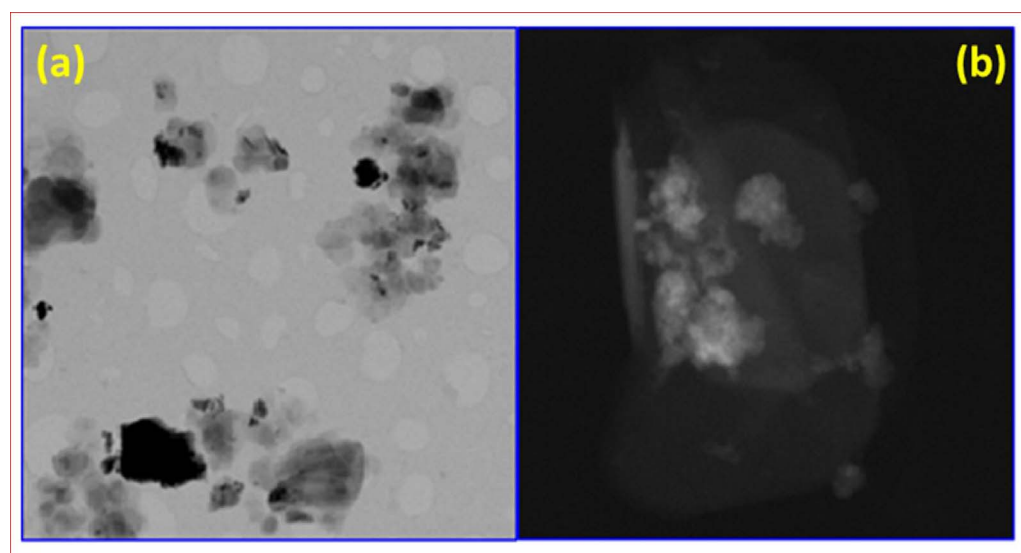


Fig. 9. SEM images of TCPIL/CuFe<sub>2</sub>O<sub>4</sub>/BNONS nanomaterial (9a), mapping of all elements in the nanomaterial (9b) mapping of individual elements.

magnetic NPs, subsequently, cation's and anions were catalytically active in nature. The bimetallic NPs such as CuFe<sub>2</sub>O<sub>4</sub> magnetic NPs also have great catalytic activity. The co-ordination or binding interactions

occur between CuFe<sub>2</sub>O<sub>4</sub> and ILs. The ILs were coated with CuFe<sub>2</sub>O<sub>4</sub> NPs as well. These copper and iron particles were strongly interacted with ILs because of its metallic charge, ionic interaction and good chelating

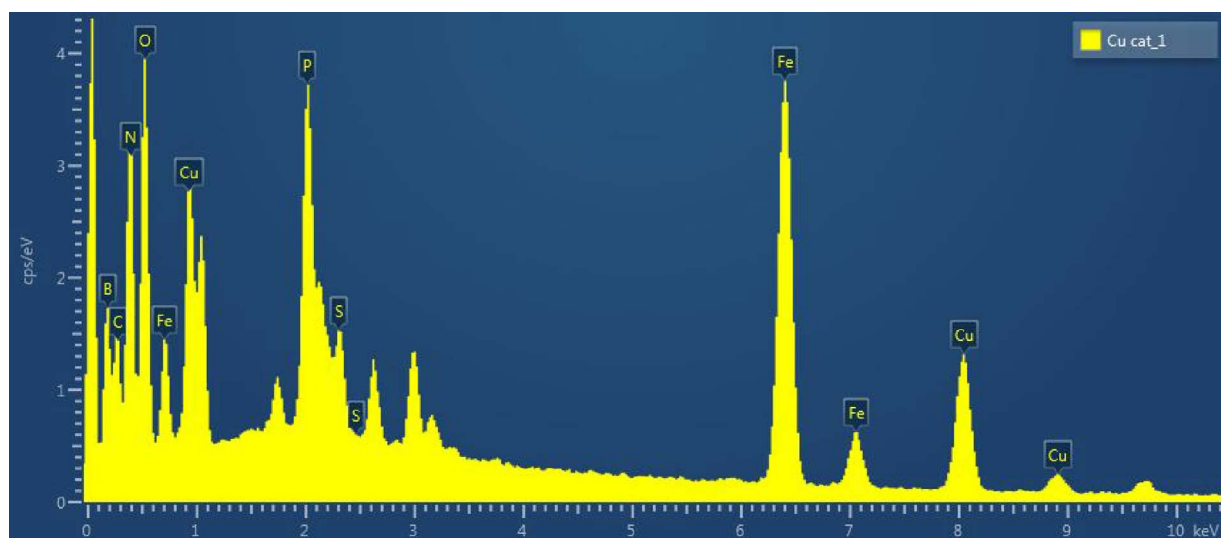
Fig. 10. EDS spectrum of TCPIL/CuFe<sub>2</sub>O<sub>4</sub>/BNONS nanomaterial.

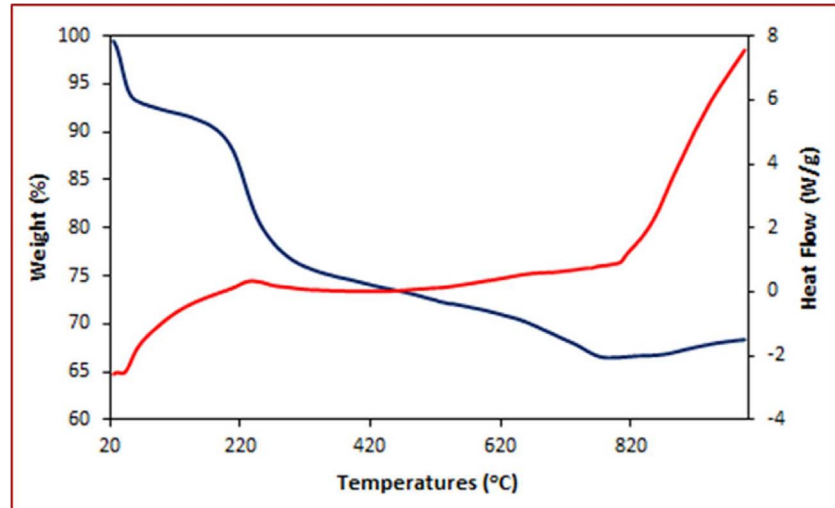
Table 1

The EDS elemental analysis results for the TCPIL/CuFe<sub>2</sub>O<sub>4</sub>/BNONS nanomaterial.

Elements	Weight %	Atomic %
B	26.24	0.98
C	13.31	0.81
N	26.60	0.60
O	16.97	0.36
P	1.70	0.05
S	0.60	0.03
Fe	8.91	0.17
Cu	5.68	0.13
Total	100	

ability of phosphonate groups in ILs. The resulting material was coated with partially oxidized BNONS because of heteroatoms such as oxygen helps to coat BNONS perfectly. This nanomaterial has good physical and chemical properties. The stability, metal identification, compositions, functional groups and morphologies were confirmed by special characterizations as discussed above. The method for preparing TCPIL/CuFe<sub>2</sub>O<sub>4</sub>/BNONS was described in an experimental. The preparation of TCPIL has three active organic molecules DABCO, N-methyl pyrrolidone and amino picoline as cations with the tri-phosphonate anion ATMP. Hence it was hypothesized that this material would expect to

have more catalytic activity. The final nanomaterial was made by these ILs capped CuFe<sub>2</sub>O<sub>4</sub> NPs through noncovalent functionalization of partially oxidized BN nanosheet because it has strong affinity with the basal plane BNONS. The main strategy for uniform and dense assembling of inorganic magnetic NPs and ILs on the BNONS was proposed to be due to the surface functionalization of BNONS with high densities of active heterocyclic compounds and phosphonate groups. The reduction of NAs was investigated with NaBH<sub>4</sub> in the absence of nanomaterial. The UV spectrum showed a slow decrease in the typical absorbance peak at 380 nm: only 3% of the NA was reduced even after 24 hrs [72] thereby suggesting that electron transfer from the donor, NaBH<sub>4</sub> to the acceptor NA might be prevented by a kinetic barrier. The catalytic activity of the prepared TCPIL/CuFe<sub>2</sub>O<sub>4</sub>/BNONS nanomaterial was evaluated for the reduction of 4-NA to PPD (*para* phenylenediamine) in the presence of NaBH<sub>4</sub>. The typical absorption peaks of 2-NA to OPD (*ortho* phenylene diamine) is at  $\lambda_{max}$  410 nm and 240 nm (Fig. 12a), 3-NA to MPD (*meta* phenylenediamine) is at 360 nm and 300 nm (Fig. 12b), 4-NA and PPD at 380 nm and 240 nm (Fig. 12c) and 4-NPDA to 2, 3, 4-triaminobenzene (Fig. 12d) at 401 nm were monitored. The absorption of MB is at  $\lambda_{max}$  300 nm, 600 nm as well as 680 nm (Fig. 12e) and AR at 500 nm (Fig. 12f) were monitored: as observed, the absorbance decreased with time corresponding to a recent report [73]. Some of the peaks in the UV spectrum was split at the top of the area due to high concentration of NAs, therefore it further explains about the

Fig. 11. TGA-DSC curve of the TCPIL/CuFe<sub>2</sub>O<sub>4</sub>/BNONS nanomaterial recorded under air atmosphere.

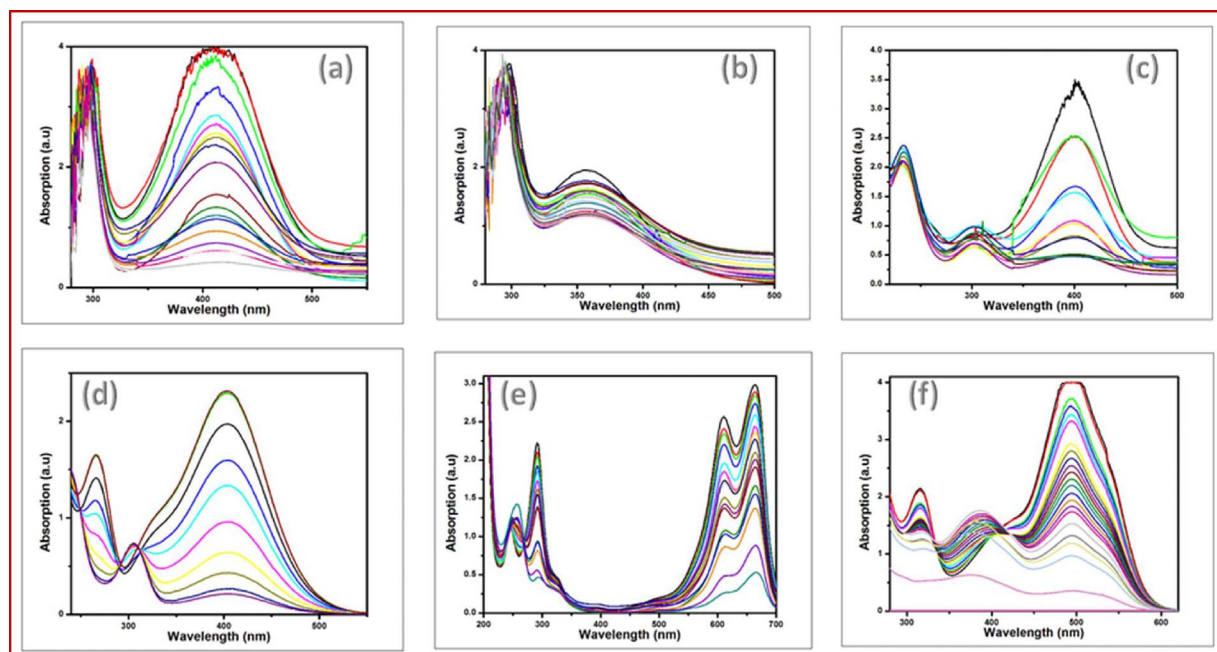


Fig. 12. UV-vis absorption spectrum for reduction reactions by nanomaterial (TCPIL/CuFe<sub>2</sub>O<sub>4</sub>/BNONS): 12a) Reduction of 2-NA to OPD 12b) Reduction of 3-NA to MPD material. 12c) Reduction of 4-NA to PPD 12d) Reduction of 4-nitro-OPD 12e) Reduction of MB dye 12f) Reduction of AR.

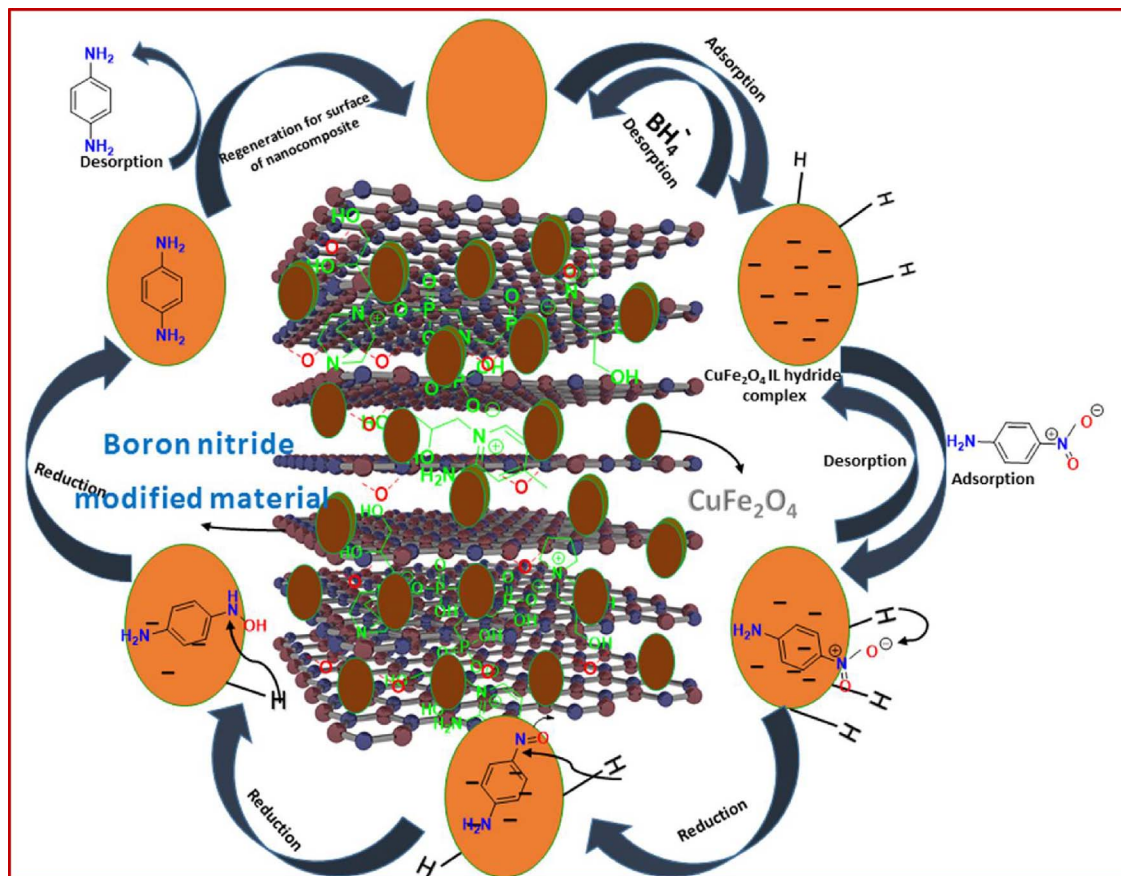


Fig. 13. Proposed mechanism for reduction of p-Nitroaniline to p-Phenylenediamine by TCPIL/CuFe<sub>2</sub>O<sub>4</sub>/BNONS nanomaterial.

catalytic activity of the nanomaterial. The catalytic activity was also compared with other BNNS supported NPs (Table ES-1). It was observed that the reduction of nitroarenes to amino-compounds using the new nanomaterial was equivalent to Pd/BNNS however the latter took a longer reaction time. The use of BNNS/Ag and Ag/BCN was reported

to cause slower reduction. To show the conversion of NAs to the amino compounds, the FTIR spectrum (Figure ES-9) was elucidated for the reduction process. Although the absorption at 1400 and 1643 cm<sup>-1</sup> for the nitro group were observed for the amino product, a significant increase of an additional amino group at 3460 cm<sup>-1</sup> was observed

thereby confirming the reduction of 4-NA (Figure ES-9).

### 3.1. Chemical kinetics for reduction reaction of series of nitroanilines and dyes

The nanomaterial IL/CuFe<sub>2</sub>O<sub>4</sub>/BNO was used as an effective catalyst to reduce a series of nitroanilines and dyes as shown in Fig. 12. The progress of the reduction reaction was indicated by the gradual decrease in the intensity in the UV spectrum of each substrate. It is suggested that due to the lower band gap of CuFe<sub>2</sub>O<sub>4</sub> NPs, the catalyst provides relatively better reduction ability. Therefore the IL most probably acts as a medium for electron movement whereas BNO and CuFe<sub>2</sub>O<sub>4</sub> can accept as well as transfer the electrons from NaBH<sub>4</sub> to the substrate investigated at room temperature. It was observed that the reduction of 2-NA, 3-NA, 4-NA, 4-NPDA, AR and MB, in the presence of the catalyst, was completed within 80, 60, 30, 50, 40 and 120 minutes, respectively. Furthermore, by increasing the temperature of the reaction, it was observed that time decreased which indicated that the reaction occurred faster. The kinetics of the reaction was determined by varying the temperature of the reactions from 25 to 60 °C and concentration of the catalyst from 0.015 to 0.045 ml (2 mg/ml). The concentration of 2-NA, 3-NA, 4-NA, 4-NPDA, AR and MB used was 0.05 M, 0.05 M, 0.05 M, 0.05 M, 0.02 M and 0.02 M, respectively, whilst aqueous NaBH<sub>4</sub> was maintained at 0.5 M. The concentration of NaBH<sub>4</sub> was significantly higher than the concentration of NAs and dyes and it was maintained constant throughout the series of reaction. The value  $C/C_0$ , measured in terms of the relative intensity of UV-vis absorbance at the specific wavelength of the substrate was obtained. The linear correlation  $\ln(C/C_0)$  or  $C/C_0$  verses reaction time, as shown in Figs. 14–17, ES.5, ES.6, ES.7 and ES.8, demonstrates the reaction to be zero-order or pseudofirst-order with respect to series of NAs and dyes concentration [75,76]. The kinetic equation for the catalytic reduction is given by  $\ln(C/C_0) = -kt$ , where  $k$  is the apparent pseudofirst-order rate constant

( $s^{-1}$ ), and  $t$  is the reaction time. The rate constant and activation energy of the reduction reaction at several temperature as well as different concentration of catalyst dose was computed and presented in Tables ES-2, ES-3 and ES-4. It was observed that  $k$  increased whilst increasing the dosage of the catalyst. The catalyst dosage of 0.015 ml (2 mg/ml) was minimal and it was the optimal dosage for the reduction reaction. For a quantitative comparison, the activity parameter  $k_0 = k/M$  was introduced, and defined as the ratio of the rate constant  $k$  to the weight of the catalyst added, where  $M$  is the total mass of the catalyst added in the reaction. Thus, the reaction rate constant per unit mass was calculated as shown in Table 2.

It was observed that the reaction mixture became turbid when higher amount of catalyst was used. This is probably due to less penetration of UV light into reaction mixture and due to light scattering thereby accounting for the decrease in the rate of the reaction. Also there is a possibility that the adsorption of product on the surface of the catalyst might block the active sites of the catalyst [74].

This investigation showed that the nanomaterials produced an excellent reduction profiles for the NAs. These results suggest that an efficient electron transfer from  $\text{BH}_4^-$  anion to NAs occurs via Fermi level shift of NPs indicating its high catalytic activity [86]. Normally, efficacy of the catalyst depends on its available active surface area and number of active sites on the surface [87]. In addition, the hydride could be formed whilst the nanomaterial reacted with borohydride and this may subsequently interacted with NA molecules which might have been adsorbed onto the metal surface [88]. Furthermore, after quick reaction at the active sites, the reaction was rapidly completed whilst the product desorbed almost immediately from the surface of the nanomaterial. On comparing the NAs used, it was observed that the reduction of 4-NPDA was quicker than 4-NA followed by 3-NA then 2-NA. Interestingly, less amount of the catalyst was used in this study compared to other reported studies. These results also suggest that the amino group might contribute significantly to the reduction reaction.

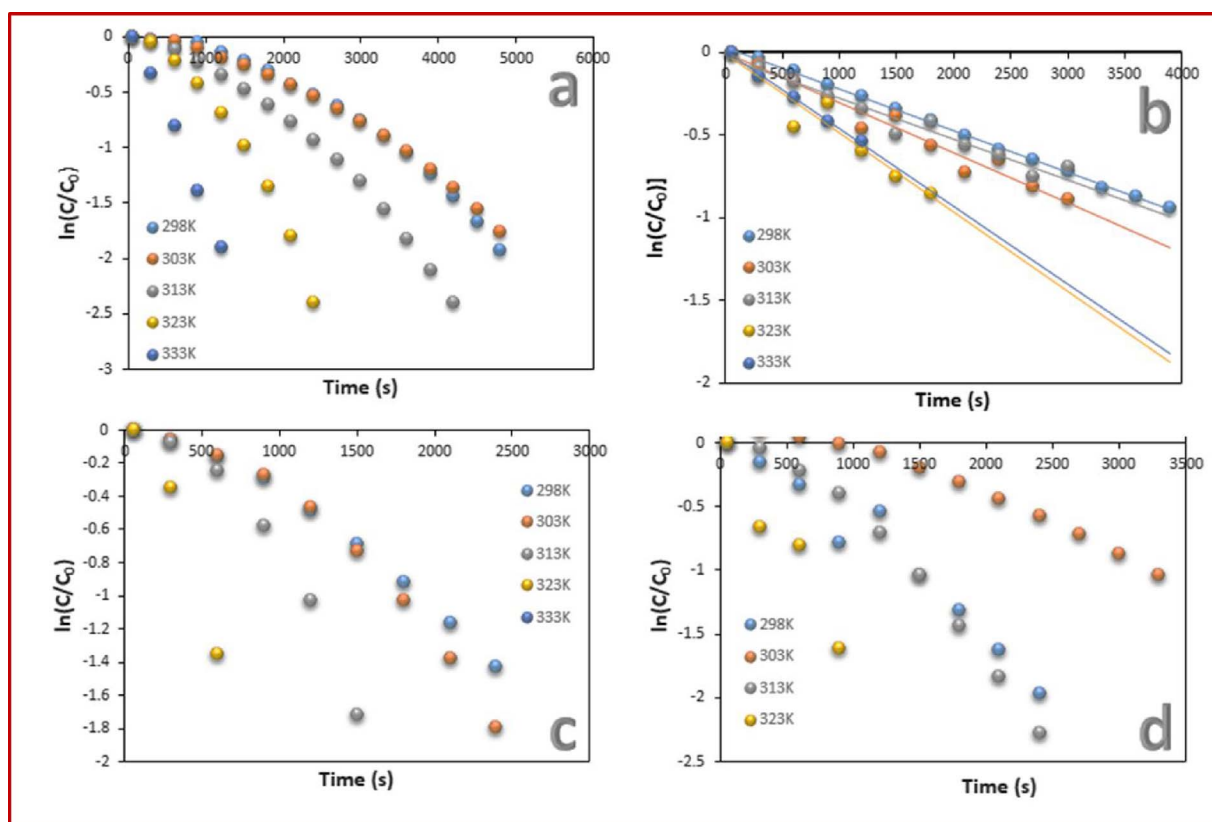


Fig. 14. Kinetic studies for reduction reaction of series of nitroanilines in presence of TCPII/CuFe<sub>2</sub>O<sub>4</sub>/BNONS at various temperatures such as 25°C, 30°C, 40 °C, 50 °C and 60 °C: a) 2-NA. b) 3-NA c) 4-NA d) 4-NPDA.

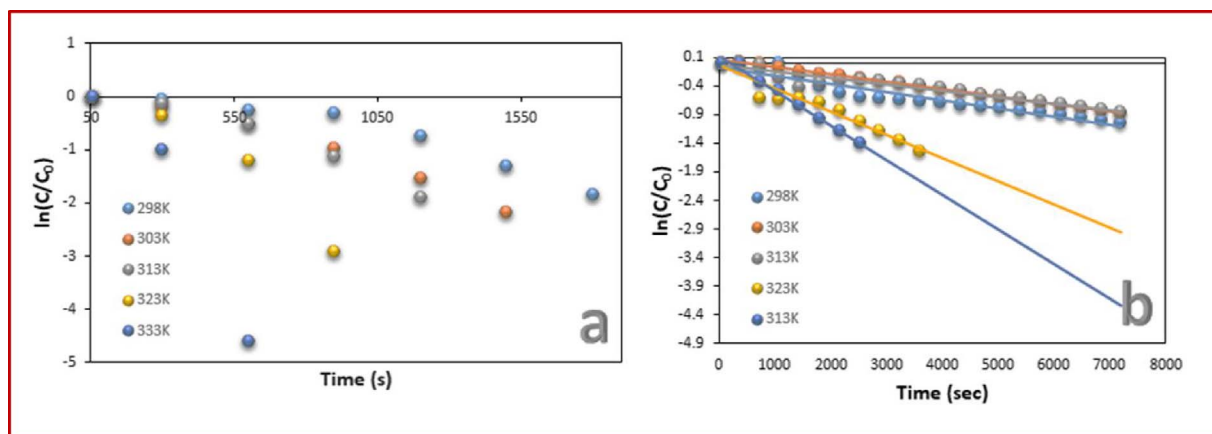


Fig. 15. Kinetic studies for reduction reaction of dyes in presence of TCPIL/CuFe<sub>2</sub>O<sub>4</sub>/BNONS at various temperatures such as 25 °C, 30 °C, 40 °C, 50 °C and 60 °C a) AR. b) MB.

Based on the position of the amino group, electron donating effect is better at the *para* and *meta* position whilst the *ortho* position takes less prominence. However 4-NPDA has an additional NH<sub>2</sub> group and therefore the electron donating contribution is the greatest (Table 3).

Several reports are available (Ref ES 1-3) on the catalytic reduction of NAs especially 2-NA and 4-NA however none is available for 3-NA. This is probably due to resistance of 3-NA against the action of catalyst because generally the 3-substituted position is more rigorous. However the nanomaterial was able to reduce all NAs easily thereby suggesting its stronger catalytic property. As a typical example, a plausible mechanism for the reduction of 4-NA to PPD (Fig. 13) is proposed. Herein the hydride ions derived from sodium borohydride initiates the reaction via CuFe<sub>2</sub>O<sub>4</sub> NPs. The IL is strongly bonded among the NPs borohydride

and BNONS, and this enhances the electron transitions: there is numerous cations and anions, so ionic moments occurs effectively. In this reaction initially due to some strong Van der Walls interaction, NA could be absorbed by BNONS and a high density of electrons stimulates more hydride ions for attacking nitro group for hydration. It is suggested that the formation of p-n junction among p-type CuFe<sub>2</sub>O<sub>4</sub> NPs and thin layered n-type BNO semiconductors in the catalyst nanomaterial probably facilitates the reduction reaction by decreasing the hole and electron recombination rate. Furthermore, the hydride ion together with the electrons are easily released from BH<sub>4</sub><sup>-</sup>. After the reduction reaction, desorption of PPD probably occurs rapidly hence allowing for the cycle to continue on the nanomaterial. In this mechanism, there is a sequential loss of water thereby promoting the reduction of the nitro

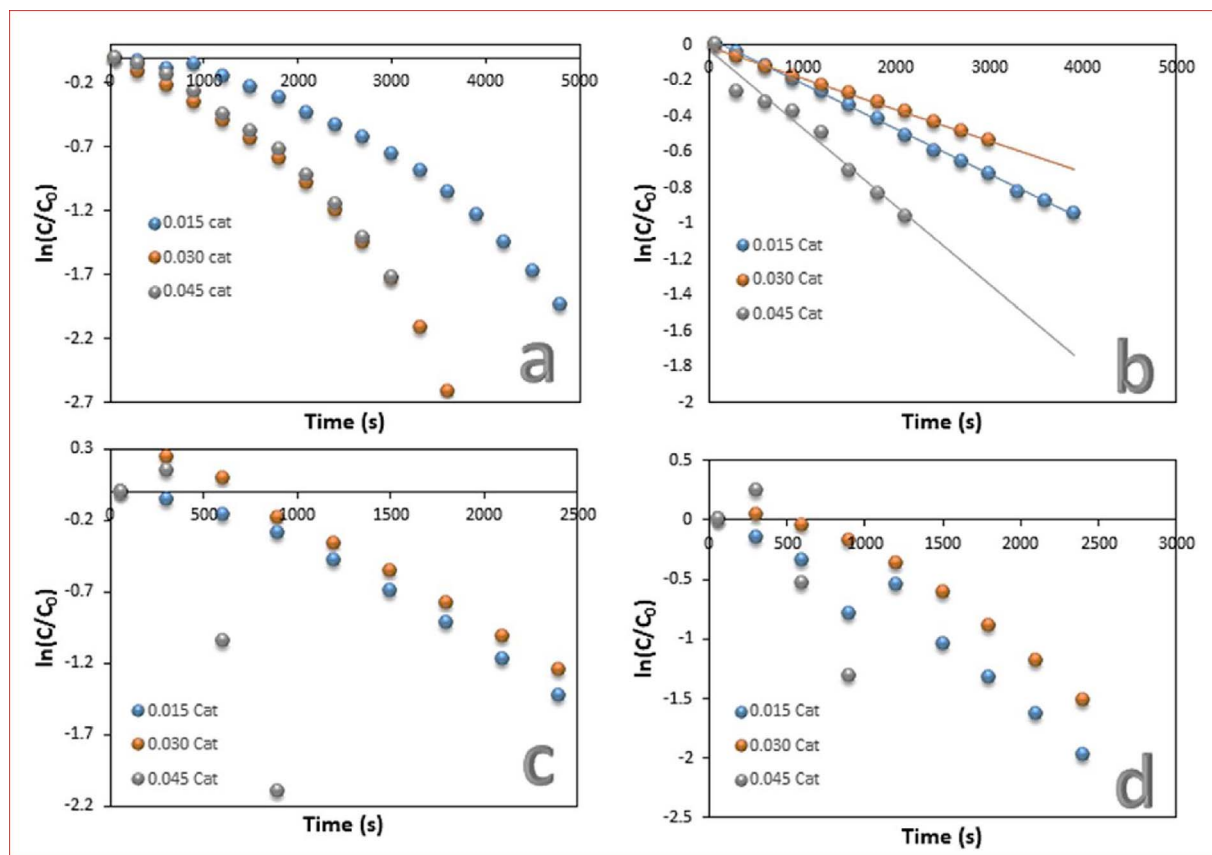


Fig. 16. Kinetic studies for reduction reaction of series of nitroanilines at various dosage of catalyst (TCPIL/CuFe<sub>2</sub>O<sub>4</sub>/BNO) such as 0.015 mL, 0.030 mL and 0.045 mL (2 mg/mL): a) 2-NA. b) 3-NA. c) 4-NA. d) 4-NPDA.

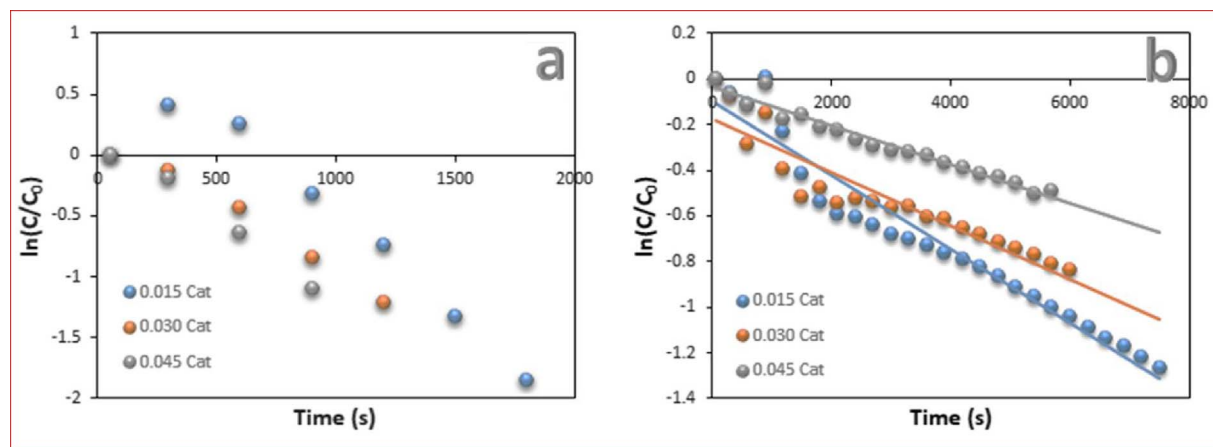


Fig. 17. Kinetic studies for reduction reaction of dyes at various dosage of catalyst (TCPIL/CuFe<sub>2</sub>O<sub>4</sub>/BNO) such as 0.015 mL, 0.030 mL and 0.045 mL (2 mg/mL): a) AR. b) MB.

Table 2

Comparison of rate constant and order of the reaction with reported catalyst.

S.NO	Catalyst	Reducing Agent	Catalyst quantity	Conversion time (in mint)	Order of the Reaction	Rate Constant (k)	Ref	Compound
1	AgNPs	NaBH <sub>4</sub>	–	55	Pseudo first order	$0.1408 \times 10^{-3} \text{ s}^{-1}$	[77]	2-NA
2	AgNPs/graphene oxide	NaBH <sub>4</sub>	–	20	Pseudo first order	$0.4384 \times 10^{-3} \text{ s}^{-1}$	[77]	2-NA
3	CuNi/Co <sub>3</sub> O <sub>4</sub>	NaBH <sub>4</sub>	2 mg	30	–	$0.78 \times 10^{-3} \text{ min}^{-1}$	[82]	2-NA
4	AgNPs/PDOP/AAOs	NaBH <sub>4</sub>	–	20	Zero order	$3.4 \times 10^{-3} \text{ M}$	[78]	2-NA
5	AgNPs	NaBH <sub>4</sub>	–	20	Zero order	$2.683 \times 10^{-4} \text{ min}^{-1}$	[79]	2-NA
6	gold nanoparticles assisted by soapnut shells extract	NaBH <sub>4</sub>	–	59	first order	$4.5 \times 10^{-2} \text{ k min}^{-1}$	[80]	4-NA
7	CuNi/Co <sub>3</sub> O <sub>4</sub>	NaBH <sub>4</sub>	2 mg	21	–	$1.71 \times 10^{-3} \text{ min}^{-1}$	[82]	4-NA
8	AgNPs/T. indica seed coat extract	NaBH <sub>4</sub>	–	10	–	$6.22 \times 10^{-3} \text{ s}^{-1}$	[81]	4-NA
9	CuNi/Co <sub>3</sub> O <sub>4</sub>	NaBH <sub>4</sub>	2 mg	30	–	$1.26 \times 10^{-3} \text{ min}^{-1}$	[82]	3-NA
10	Ag <sub>50</sub> Ni <sub>50</sub> /RGO nanocomposites	NaBH <sub>4</sub>	–	0.2	–	$1.79 \times 10^{-4} \text{ s}^{-1}$	[83]	3-NA
11	12.5Cu @ SBA-15	NaBH <sub>4</sub>	–	8	Pseudo first order	$0.56 \text{ min}^{-1}$	[84]	MB
12	gold nanoparticles capped by salmalia malabarica gum	NaBH <sub>4</sub>	–	9	Pseudo first order	$0.241 \text{ min}^{-1}$	[85]	MB
13	TCPIL/CuFe <sub>2</sub> O <sub>4</sub> /BNO	NaBH <sub>4</sub>	0.015 ml (2 mg/ml)	80	Zero order	$1.93 \times 10^{-4} \text{ M s}^{-1}$	This work	2-NA
14	TCPIL/CuFe <sub>2</sub> O <sub>4</sub> /BNO	NaBH <sub>4</sub>	0.015 ml (2 mg/ml)	65	Pseudofirst order	$2.52 \times 10^{-4} \text{ s}^{-1}$	This work	3-NA
15	TCPIL/CuFe <sub>2</sub> O <sub>4</sub> /BNO	NaBH <sub>4</sub>	0.015 ml (2 mg/ml)	40	Zero order	$3.43 \times 10^{-4} \text{ M s}^{-1}$	This work	4-NA
16	TCPIL/CuFe <sub>2</sub> O <sub>4</sub> /BNO	NaBH <sub>4</sub>	0.015 ml (2 mg/ml)	40	Zero order	$3.6 \times 10^{-4} \text{ M s}^{-1}$	This work	4-Nitro-2-Phenylenediamine
17	TCPIL/CuFe <sub>2</sub> O <sub>4</sub> /BNO	NaBH <sub>4</sub>	0.015 ml (2 mg/ml)	120	Pseudo first order	$1.44 \times 10^{-4} \text{ s}^{-1}$	This work	MB
18	TCPIL/CuFe <sub>2</sub> O <sub>4</sub> /BNO	NaBH <sub>4</sub>	0.015 ml (2 mg/ml)	50	Zero order	$7.15 \times 10^{-4} \text{ M s}^{-1}$	This work	Allura red

Table 3

Kinetic studies of rate constant, order of the reaction, ratio constant and activation energy.

S.No	Compound	Quantity of Catalyst (mg)	Order of the Reaction	Rate Constant	Ratio Constant (s <sup>-1</sup> g)	Activation Energy (10 <sup>-4</sup> KJmol <sup>-1</sup> )
1	2-NA	0.3	Zero-Order	$1.93 \times 10^{-4} \text{ M s}^{-1}$	0.6433	2.94
2	3-NA	0.3	Pseudofirst-Order	$2.52 \times 10^{-4} \text{ s}^{-1}$	0.8400	1.31
3	4-NA	0.3	Zero-Order	$3.43 \times 10^{-4} \text{ M s}^{-1}$	1.1433	7.74
4	4-Nitro-2-phenylenediamine	0.3	Zero-Order	$3.6 \times 10^{-4} \text{ M s}^{-1}$	1.2000	1.14
5	Allura red	0.3	Zero-Order	$7.15 \times 10^{-4} \text{ M s}^{-1}$	2.3833	5.96
6	Methylene blue	0.3	Pseudofirst-Order	$1.62 \times 10^{-4} \text{ s}^{-1}$	0.5400	2.58

group. Furthermore, the nanomaterial did not show any loss in its catalytic activity even after being re-used for seven times, revealing its good reusability. It is expected that the greater catalytic performance of the TCPIL/CuFe<sub>2</sub>O<sub>4</sub>/BNONS nanomaterial can be elucidated as follows: (a) BNONS exhibit excellent physicochemical properties as that of its structural analogue, graphene and the multi heterocyclic structure of phosphonate IL enable NA to absorb via ionic interactions, resulting in a high concentration of NA near the CuFe<sub>2</sub>O<sub>4</sub> bimetallic NPs on the

surface of the BNONS (b) The small size of NPs and uniform distribution of ILs on the surface of BNONS led to an efficient catalytic reaction.

The difference of morphologies between NP and IL may be related to the oxidation-reduction potential and dosage of the copper and iron metal ions. The nanomaterial acted as a medium to relay the electrons from the donor NaBH<sub>4</sub> to the acceptor NA and dye molecule thereby facilitating the reduction reaction. Due to their greater surface area, high electron density and charge dispersion, the hydride ion, after

electron transfer to the material, approaches NAs to reduce it to PDs [89–91]. Two main parameters are important for catalytic activity of material, viz., the surface area available for electron transfer and the catalyst active sites on the surface for the electron transfer thereby removing the kinetic barrier [92].

#### 4. Conclusions

In conclusion, a novel tri-cationic phosphonate IL, with different heterocyclic cations, was successfully synthesized and characterized. Furthermore, a partially oxidized BNONS and CuFe<sub>2</sub>O<sub>4</sub>NP were prepared and subsequently used to prepare a novel nanomaterial TCPIL/CuFe<sub>2</sub>O<sub>4</sub>/BNONS which was characterized by techniques such as FTIR, XRD, SEM, EDS, TEM, HRTEM, STEM, ED, XPS, AFM and DSC-TGA. This nanomaterial was effectively used as a heterogeneous catalyst for the efficient reduction of series of NAs to corresponding PDs, as well as for AR and MB. From kinetic studies, the rate constant, order of the reaction, constant ratio and activation energy was computed. Furthermore kinetic studies at various temperatures showed that an increase in temperature speeded the reaction whilst by increasing the amount of catalyst the reaction also occurred faster. The recovery and reusability (see Figure ES-10) of the nanomaterial is simple and performs well in aqueous solution, without heating or reducing agent and without the use of any special equipment. Moreover, it is possible to make different nanomaterials by combining different d-block metals such Zn, Pd, Pt and Mn with BNONSs for potential applications in biomedical, sensors and catalytic fields.

#### Acknowledgements

Mr. Vasanthakumar Arumugam is grateful to the National Research Foundation of the Innovation Doctoral Scholarship (Grant no: 1011117 & 109839) for financial support and Durban University of Technology for providing a good environment and laboratory facilities for this work. Special thanks to Dr. T Singh, Department of Chemistry, Durban University of Technology for assisting with the kinetic studies aspects.

Note: This work is pending a patent.

#### Appendix A. Supplementary data

Supplementary data associated with this article can be found, in the online version, at <http://dx.doi.org/10.1016/j.apcatb.2017.08.059>.

#### References

- [1] J.P. Hallett, T. Welton, *Chem. Rev.* 111 (2011) 3508–3576.
- [2] T. Welton, *Chem. Rev.* 99 (1999) 2071–2083.
- [3] M. Armand, F. Endres, D.R. MacFarlane, H. Ohno, B. Scrosati, *Nat. Mater.* 8 (2009) 621–629.
- [4] B.H. Xu, J.Q. Wang, J. Sun, Y. Huang, J.P. Zhang, X.P. Zhang, S.J. Zhang, *Green Chem.* 17 (2015) 108–122.
- [5] G. Fiorani, W. Guo, A.W. Kleij, *Green Chem.* 17 (2015) 1375–1389.
- [6] W.E.S. Hart, J.B. Harper, L. Aldous, *Green Chem.* 17 (2015) 214–218.
- [7] M. Taha, A.M.R. Imeida, F.A.E. Silva, P. Domingues, S.P.M. Ventura, J.A.P. Coutinho, M.G. Freire, *J. Chem. Eur.* 21 (2015) 4781–4788.
- [8] J.W. Comerford, I.D.W. Ingram, M. North, X. Wu, *Green Chem.* 17 (2015) 1966.
- [9] A. Taheri, B. Lai, C. Cheng, Y. Gu, *Green Chem.* 17 (2015) 812.
- [10] S. Zhang, K. Dokko, M. Watanabe, *Chem. Sci.* 6 (2015) 3684.
- [11] G. Godeau, L. Navailles, F. Nallet, X. Lin, T.J. McIntosh, M.W. Grinstaff, *Macromolecules* 45 (2012) 2509–2513.
- [12] M. Wathier, M.W. Grinstaff, *Macromolecules* 43 (2010) 9529–9533.
- [13] M. Wathier, M.W. Grinstaff, *J. Am. Chem. Soc.* 130 (2008) 9648–9649.
- [14] G. Kamath, G.A. Baker, *RSC Adv.* 3 (2013) 8197–8202.
- [15] J. Luo, N. Zhang, R. Liu, X. Liu, *RSC Adv.* 4 (2014) 64816–64824.
- [16] Y. Mo, Y. Wan, A. Chau, F. Huang, *Sci. Rep.* 4 (2014) 1–8.
- [17] A. Marimuthu, J. Zhang, S. Linic, *Science* 339 (2013) 1590–1593.
- [18] J. Wang, K. Wang, F.B. Wang, X.H. Xia, *Nat. Commun.* 5 (2014) 1–9.
- [19] A.M. Hengge, C.V. Rode, *Green. Chem.* 14 (2012) 1064–1072.
- [20] A. Fornara, P. Johansson, K. Petersson, S. Gustafsson, J. Qin, E. Olsson, D. Ilver, A. Krozer, M. Muhameed, C. Johansson, *Nano Lett.* 8 (2008) 3423–3428.
- [21] R.S. Singh, R.Y. Tay, W.L. Chow, S.H. Tsang, G. Mallick, E.H.T. Teo, *Appl. Phys. Lett.* 104 (2014) 163101.
- [22] L.H. Li, J. Cervenka, K. Watanabe, T. Taniguchi, Y. Chen, *ACS Nano* 8 (2014) 1457–1462.
- [23] A. Pakdel, C. Zhi, Y. Bando, D. Golberg, *Mater. Today* 15 (2012) 256–265.
- [24] W. Lei, D. Portehault, D. Liu, S. Qin, Y. Chen, *Nat. Commun.* 4 (2013) 1–7.
- [25] I. Jo, M.T. Pettes, J. Kim, K. Watanabe, T. Taniguchi, Z. Yao, L. Shi, *Nano Lett.* 13 (2013) 550–554.
- [26] G.H. Yang, J.J. Shi, S. Wang, W.W. Xiong, L.P. Jiang, C. Burda, J.J. Zhu, *Chem. Commun.* 49 (2013) 10757–10759.
- [27] X. Chen, W. Zang, K. Vimalanathan, K.S. Iyer, C.L. Raston, *Chem. Commun.* 49 (2013) 1160–1162.
- [28] C. Huang, C. Chen, X. Ye, W. Ye, J. Hu, C. Xu, X. Qiu, *J. Mater. Chem. A* 1 (2013) 12192–12197.
- [29] X. Wang, G. Meng, C. Zhu, Z. Huang, Y. Qian, K. Sun, X. Zhu, *Adv. Funct. Mater.* 23 (2013) 5771–5777.
- [30] C. Huang, W. Ye, Q. Liu, X. Qiu, *ACS Appl. Mater. Interfaces* 6 (2014) 14469–14476.
- [31] Q. Fu, Y. Meng, Z. Fang, Q. Hu, L. Xu, W. Gao, X. Huang, Q. Xue, Y.P. Sun, F. Lu, *ACS Appl. Mater. Interfaces* 9 (2017) 2469–2476.
- [32] Y. Guo, W. Guo, *Phys. Chem. Chem. Phys.* 17 (2015) 16428–16433.
- [33] J. Wu, L. Yin, *ACS Appl. Mater. Interfaces* 3 (2011) 4354–4362.
- [34] H. Shen, D. Cuan, J. Guo, N. Zhao, J. Xu, *J. Mater. Chem. A* 3 (2015) 16663–16669.
- [35] Y. Lin, C.E. Bunker, K.A.S. Fernando, J.W. Connell, *ACS Appl. Mater. Interfaces* 4 (2012) 1110–1117.
- [36] S. Dutta, C. Ray, S. Sarkar, M. Pradhan, Y. Negishi, T. Pal, *ACS Appl. Mater. Interfaces* 5 (2013) 8724–8732.
- [37] L. Pan, Y.T. Liu, X.M. Xie, X.D. Zhu, *J. Chem. Asian* 9 (2014) 1519–1524.
- [38] X. Huang, B. Zheng, Z. Liu, C. Tan, J. Liu, B. Chen, H. Li, J. Chen, X. Zhang, Z. Fan, W. Zhang, Z. Guo, F. Huo, Y. Yang, L. Xie, W. Huang, H. Zhang, *ACS Nano* 8 (2014) 8695–8701.
- [39] M. Srivastava, A.K. Das, P. Khanra, M.E. Uddin, N.H. Kim, J.H. Lee, *J. Mater. Chem. A* 1 (2013) 9792–9801.
- [40] W. Wang, J. Gu, W. Hua, X. Jia, K. Xi, *Chem. Commun.* 50 (2014) 8889–8891.
- [41] M. Ayan-Varela, M.J. Fernandez-Merino, J.I. Paredes, S. Villar-Rodil, C. Fernandez-Sanchez, L. Guardia, A. Martinez-Alonso, J.M.D. Tascon, *J. Mater. Chem. A* 2 (2014) 7295–7305.
- [42] J.J. Lv, A.J. Wang, X. Ma, R.Y. Xiang, J.R. Chen, J.J. Feng, *J. Mater. Chem. A* 3 (2015) 290–296.
- [43] Y. Yan, B. Xia, Z. Xu, X. Wang, *ACS Catal.* 4 (2014) 1693–1705.
- [44] G.H. Gao, A. Mathkar, E.P. Martins, D.S. Galvao, D.Y. Gao, P.A.D. Autreto, C.J. Sun, L.T. Cai, P.M. Ajayan, *J. Mater. Chem. A* 2 (2014) 3148–3154.
- [45] W. Shao, X. Liu, H. Min, G. Dong, Q. Feng, S. Zuo, *ACS Appl. Mater. Interfaces* 7 (2015) 6966–6973.
- [46] C. Zhi, N. Hanagata, Y. Bando, D. Golberg, *J. Chem. Asian* 6 (2011) 2530–2535.
- [47] R.J. Smith, P.J. King, M. Lotya, C. Wirtz, U. Khan, S. De, A. O'Neill, G.S. Duesberg, J.C. Grunlan, G. Moriarty, J. Chen, J. Wang, A.I. Minett, V. Nicolosi, J.N. Coleman, *Adv. Mater.* 23 (2011) 3944–3948.
- [48] J.L. Li, K.N. Kudin, M.J. McAllister, R.K. Prud'hommed, A.A. Aksay, R. Car, *Phys. Rev. Lett.* 96 (2006) 176101.
- [49] A. Ying, Z. Li, J. Yang, S. Liu, S. Xu, H. Yan, C. Wu, *J. Org. Chem.* 79 (2014) 6510–6516.
- [50] R. Hudson, Y. Feng, R.S. Varma, A. Moores, *Green Chem.* 16 (2014) 4493–4505.
- [51] A. Schejn, T. Mazet, V. Falk, L. Balan, L. Aranda, G. Medjahdi, R. Schneider, *Dalton Trans.* 44 (2015) 10136–10140.
- [52] S. Kotake, T. Hasegawa, K. Kamiya, Y. Suzuki, T. Masui, Y. Kangawa, *Appl. Surf. Sci.* 216 (2003) 72–77.
- [53] S. Palaniappan, B. Boddula, B. Ravi, *J. Appl. Polym. S.C.I.* 130 (2013) 2995–3000.
- [54] C.Y. Zhi, Y. Bando, C.C. Tang, D. Golberg, *Appl. Phys. Lett.* 86 (2005) 213110.
- [55] J. Yu, Z. Zheng, H.C. Ong, K.Y. Wong, S. Matsumoto, W.M. Lau, *J. Phys. Chem. B* 110 (2006) 21073–21076.
- [56] A.L.M. Reddy, A.E. Tanur, G.C. Walker, *Int. J. Hydrogen Energy.* 35 (2010) 4138–4143.
- [57] F. Guo, Y.H. Ni, Y. Ma, N.N. Xiang, C. Liu, *New J. Chem.* 38 (2014) 5324–5330.
- [58] Z.H. Farooqi, K. Naseem, R. Begum, A. Ijaz, *J. Inorg. Organomet. Polym. Mater.* 25 (2015) 1554–1568.
- [59] K. Li, Z. Zheng, X. Huang, G. Zhao, J. Feng, J. Zhang, *J. Hazard. Mater.* 166 (2009) 213–220.
- [60] Z. Dong, X. Le, X. Li, W. Zhang, C. Dong, J. Ma, *Appl. Catal. B* 158–159 (2014) 129–135.
- [61] S. Gazi, R. Ananthakrishnan, *Appl. Catal. B* 105 (2011) 317–325.
- [62] L. Li, Y. Feng, Y. Liu, B. Wei, J. Guo, W. Jiao, Z. Zhang, Q. Zhang, *Appl. Surf. Sci.* 363 (2016) 627–635.
- [63] S.M. El-Sheikh, A.A. Ismail, J.F. Al-Sharab, *New J. Chem.* 37 (2013) 2399–2407.
- [64] N.M. Patil, T. Sasaki, B.M. Bhanage, *ACS Sustainable Chem. Eng.* 4 (2016) 429–436.
- [65] R.N. Muthu, S. Rajashabala, R. Kannan, *Renew. Energy.* 85 (2016) 387–394.
- [66] V. Linss, S. Rodilb, P. Reinke, M. Garnier, P. Oelhafend, U. Kreissige, F. Richtera, *Thin Solid Films.* 467 (2004) 76–87.
- [67] M.A. Mannan, M. Nagano, T. Kida, N. Hirao, Y. Baba, *J. Phys. Chem. Solids.* 7 (2009) 20–25.
- [68] S.Y. Kim, J. Park, H.C. Choi, J.P. Ahn, J.Q. Hou, H.S. Kang, *J. Am. Chem. Soc.* 129 (2007) 1705–1716.
- [69] F.L. Huang, C.B. Cao, X. Xiang, R.T. Lv, H.S. Zhu, *Mater.* 13 (2004) 1757–1760.
- [70] J. Gao, P.K. Chow, A.V. Thomas, T.M. Lu, T. Borca-Tasciuc, N. Koratkar, *Appl. Phys. Lett.* 105 (2014) 123108.
- [71] Y. Lin, J.W. Connell, *Nanoscale* 4 (2012) 6908–6939.

[72] M.A.A. Ahmed, S.R. Torati, C. Kim, *Nanoscale* 7 (2015) 12192–12204.

[73] K. Bahar, B. Maryam, N. Mahmoud, *L Achillea millefolium*, *Journal of Colloid and Interface Science* 493 (2017) 85–93.

[74] T. Zeng, H. Niu, Y. Ma, W. Li, Y. Cai, *Appl Catal. B: Environ.* 134–135 (2013) 26–33.

[75] H. Gu, J. Wang, Y. Ji, Z. Wang, W. Chen, G. Xue, *J. Mater. Chem. A* 1 (2013) 12471–12477.

[76] W. Hu, B. Liu, Q. Wang, Y. Liu, Y. Liu, P. Jing, S. Yu, L. Liu, J. Zhang, *Chem. Commun.* 49 (2013) 7596–7598.

[77] Y. Zhang, X. Yuan, Y. Wang, Y. Chen, *J. Mater. Chem.* 22 (2012) 7245–7251.

[78] B. Celen, D. Ekiz, E. Piskin, G. Demirel, *J. Mol. Catal. A: Chem.* 350 (2011) 97–102.

[79] T.V. Thu, P.J. Ko, N.H.H. Phuc, A. Sandhu, *J. Nanopart. Res.* 15 (2013) 1975.

[80] V. Reddy, R.S. Torati, S. Oh, C. Kim, *Industrial & Engineering Chemistry Research* 52 (2) (2013) 556–564.

[81] T.N.J.I. Edison, M.G. Sethuraman, Y.R. Lee, *Research on Chemical Intermediates* 42 (2) (2016) 713–724.

[82] P. Deka, R. Choudhury, R.C. Deka, P. Bharali, *R.S.C Advances* 6 (75) (2016) 71517–71528.

[83] R. Dhanda, M. Kidwai, *J. Mat Chem A* 3 (38) (2015) 19563–19574.

[84] B.K. Ghosh, S. Hazra, B. Naik, N.N. Ghosh, *Powder Technology* 269 (2015) 371–378.

[85] B.R. Ganapuram, M. Alle, R. Dadigala, A. Dasari, V. Maragoni, V. Guttena, *International Nano Letters* 5 (4) (2015) 215–222.

[86] M. Jakob, H. Levanon, *NanoLett.* 3 (2003) 353–358.

[87] D. Huang, X. Bai, L. Zheng, *J. Phys Chem C* 115 (2011) 14641–14647.

[88] Q. Zhou, G. Qian, Y. Li, G. Zhao, Y. Chao, J. Zheng, *Thin Solid Films* 516 (2008) 953–956.

[89] M. Kumar, S. Deka, *ACS Appl. Mater. Interfaces* 6 (2014) 16071–16081.

[90] X. Du, J. He, J. Zhu, L. Sun, S. An, *Applied Surface Science* 258 (2012) 2717–2723.

[91] B. Naik, S. Hazra, V.S. Prasad, N.N. Ghosh, *Catal. Commun.* 12 (2011) 1104–1108.

[92] S. Kundu, M. Jayachandran, *RSC Adv.* 3 (2013) 16486–16498.